Simulating functional magnetic materials on supercomputers

2009 J. Phys.: Condens. Matter 21 293201

(http://iopscience.iop.org/0953-8984/21/29/293201)

IOP PUBLISHING JOURNAL OF PHYSICS: CONDENSED MATTER

J. Phys.: Condens. Matter **21** (2009) 293201 (31pp) doi:10.1088/0953-8984/21/29/293201

TOPICAL REVIEW

Simulating functional magnetic materials on supercomputers

Markus Ernst Gruner and Peter Entel

Physics Department and Centre for Nanointegration CENIDE, University of Duisburg-Essen, Duisburg Campus, 47048 Duisburg, Germany

E-mail: Markus.Gruner@uni-due.de and Peter.Entel@uni-due.de

Received 24 January 2009, in final form 8 May 2009
Published 29 June 2009
Online at stacks.iop.org/JPhysCM/21/293201

Abstract

The recent passing of the petaflop per second landmark by the Roadrunner project at the Los Alamos National Laboratory marks a preliminary peak of an impressive world-wide development in the high-performance scientific computing sector. Also, purely academic state-of-the-art supercomputers such as the IBM Blue Gene/P at Forschungszentrum Jülich allow us nowadays to investigate large systems of the order of 10^3 spin polarized transition metal atoms by means of density functional theory. Three applications will be presented where large-scale *ab initio* calculations contribute to the understanding of key properties emerging from a close interrelation between structure and magnetism. The first two examples discuss the size dependent evolution of equilibrium structural motifs in elementary iron and binary Fe–Pt and Co–Pt transition metal nanoparticles, which are currently discussed as promising candidates for ultra-high-density magnetic data storage media. However, the preference for multiply twinned morphologies at smaller cluster sizes counteracts the formation of a single-crystalline $L1_0$ phase, which alone provides the required hard magnetic properties. The third application is concerned with the magnetic shape memory effect in the Ni–Mn–Ga Heusler alloy, which is a technologically relevant candidate for magnetomechanical actuators and sensors. In this material strains of up to 10% can be induced by external magnetic fields due to the field induced shifting of martensitic twin boundaries, requiring an extremely high mobility of the martensitic twin boundaries, but also the selection of the appropriate martensitic structure from the rich phase diagram.

(Some figures in this article are in colour only in the electronic version)

Contents

1. Introduction

The increasing trend towards miniaturization of everyday-life goods provides smart materials with an increasingly important role in technological applications. A specific group of smart

materials is functional magnetic materials, where in the widest sense of the definition the magnetic properties determine the functional applications. In many cases, the desired functional magnetic properties of these materials are connected with a specific structural conformation relying on the absence and sometimes also the presence of structural defects (for an overview, see, for example [1]). The detailed understanding of the specific interplay of magnetic and structural properties is thus decisive for the optimization of functional materials or even the design of new alloys and compounds for a given purpose.

Magnetic nanoparticles, for instance, play an important role in biomedical applications, as carriers for targeted drug delivery within the human body or as heating agents for local hypothermic cancer treatment strategies [2–4]. Other potential applications envisage their use as building blocks for ultra-high-density magnetic data storage media [5, 6]. Here, in particular, a large magnetocrystalline anisotropy is required, assuring a stability of the stored information of the order of decades. For the case of Fe–Pt and Co–Pt, the largest magnetocrystalline anisotropy is expected for single-crystalline particles of the $L1_0$ phase, which exhibits extremely large values in the bulk [7]. The occurrence of so-called multiple twinning, which is induced by a competition between surface and core energies and typical for small particle sizes, counteracts the required large magnetocrystalline anisotropy and thus the miniaturization of the bits by reducing the particle sizes down to a few nanometres. In contrast, in magnetic shape memory materials, a prerequisite for their functional purpose is the existence of a martensitic phase and in consequence the presence of internal interfaces such as twin boundaries (see, e.g., [1, 8–10]). Their extremely large mobility in combination with a considerable magnetocrystalline anisotropy allows shifting by moderate magnetic fields of the order of 1 T, which in consequence leads to a huge macroscopic change of shape in the range of several per cent in the lateral dimensions.

The investigation of atomistic processes in the above mentioned materials should cover at least a few nanometres, requiring system sizes of the order of 10^2–10^3 atoms. Traditionally, this is the realm of classical statistical methods such as molecular dynamics simulations using empirical inter-atomic potentials or semi-empirical quantum-mechanical approaches such as tight-binding schemes (e.g. [11–16]). These methods usually rely on careful fitting procedures to material-specific quantities, which must be obtained from experiment or *ab initio* calculations, and lack in general the accuracy to give a definitive account of the interrelation of the electronic and structural properties, without benchmarking against a higher level of theory or experiment. This is especially true for systems with a strong interplay of magnetic and structural properties such as those which are the main topic of this review. For gaining insight into dynamical processes on realistic timescales or the investigation of thermodynamical properties, calculations based on classical empirical methods are indispensable, nevertheless. *Ab initio* calculations in the framework of the density functional theory provide the required accuracy but are on the other hand computationally expensive and thus traditionally limited to rather small system sizes. Therefore, in recent times, efforts have been made to improve the classical simulation schemes, e.g. by incorporating magnetic degrees of freedom into classical simulations of real materials on a systematic basis [17, 18]. A very promising route is the development of so-called $\mathcal{O}(N)$ DFT methods [19–24]. These provide like classical molecular dynamics a linear increase of the computational demands with the system size, allowing system sizes N larger than 10^5 to be considered. Most of these approaches work best for semiconductors and insulators, as they require a rather close localization of orbitals at the atomic positions. To the authors' knowledge, extensive investigations of structural properties of large transition metal systems have not been reported so far.

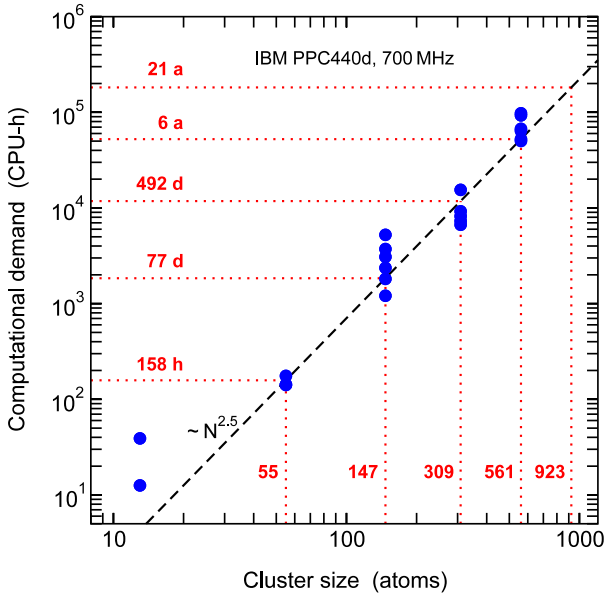

Figure 1. Double logarithmic plot of the computation time per CPU needed on JUBL for a full geometric optimization of Fe–Pt nanoclusters of magic cluster sizes according to equation (8). Originally published in [25].

For problems like the ones discussed in this review, it is therefore still unavoidable to come back to traditional DFT implementations, although they are hampered by a much worse scaling behaviour. For the example discussed in section 4, this is shown in figure 1. A full structural optimization of a Fe–Pt nanocluster with 561 atoms would require several years of computing time, if performed on a single processor machine; a particle of the order of 10^3 atoms would even take decades. This clearly demonstrates that such calculations are only possible on massively parallel supercomputers, using 1000 processors or more at the same time. This has become possible by the recent development in the supercomputing sector over the last 15 years leading to an amazing exponential overall increase in capacity, doubling the world-wide available computing power nearly every 13 months (cf figure 2). Another important trend visible from figure 2 is that the improvement in the average performance per processor lost momentum during the past decade in favour of massively parallelized machines containing thousands of processor cores.

The increasing availability of large computational resources has allowed the physical problems to grow larger, as

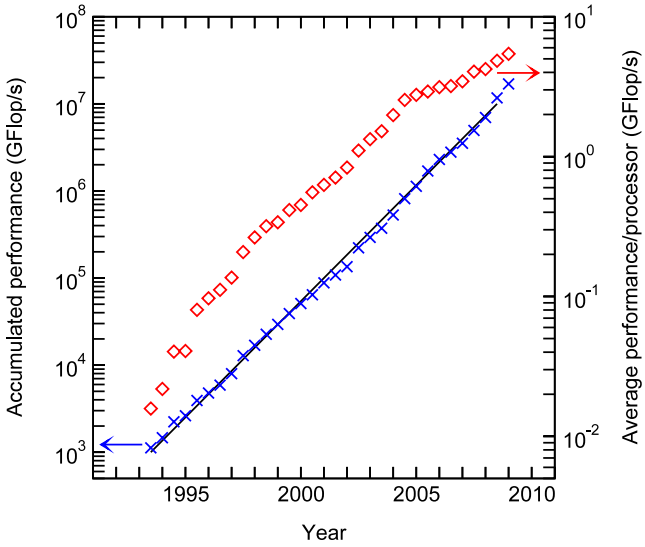

Figure 2. Evolution of the accumulated available theoretical performance (maximum measured Linpack power in units of 10^9 floating point operations per second) and averaged performance per processor (as given by the accumulated performance divided by the total number of processors) of the world's 500 fastest supercomputers within the last 15 years (data by kind permission of the TOP500 project). The collection comprises academic as well as non-academic (e.g. commercial and military) sites; see the TOP500 web-site for more information [26].

several examples from materials science impressively demonstrate, e.g. the simulation of extended carbon nanostructures [27], the investigation of Pd-nanowire self-assembly from individual Pd_{225} nanoparticles [28], and the simulation of structural phase transitions in Ge/Sb/Te phase-change materials for optical data recording purposes [29, 30] with up to 460 atoms or the exemplary electronic structure calculation of a supercell containing 1000 molybdenum atoms [31, 32]. Another outstanding work is the determination of structural and electronic properties of a boron nitride nano-mesh placed on a rhodium substrate considering more than 1100 atoms within a full potential approach [33, 34].

Within this contribution we will present three more showcases, where large-scale DFT calculations contribute to the advance in the field of materials science, with a special emphasis on functional magnetic materials. The calculations were performed on more than 1000 processors on the IBM Blue Gene installations of the John von Neumann Institute for Computing at Forschungszentrum Jülich and cover *ab initio* structure optimizations of up to 923 spin-polarized transition metal atoms.

2. Technical details and performance

Determining materials properties from first principles requires nothing less than solving the Schrödinger equation for a system of several thousand electrons interacting with the nuclei and each other. The solution is described in terms of a many-body wavefunction, depending explicitly on the coordinates of all considered electrons. In practice, this can be approximated by a finite combination of single-electron wavefunctions. Modern quantum chemical methods can accomplish this task with nearly arbitrary accuracy, but the price is a prohibitive scaling of the computational resources with the system size. The elegant way out is to describe the problem in terms of the electronic density, $n(\underline{r})$, instead, which is sufficient to uniquely determine the ground state energy as laid out by Hohenberg and Kohn more than four decades ago [35, 36].

$$E[n(\underline{r})] = T_0[n(\underline{r})] + \int \mathrm{d}\underline{r}\, n(\underline{r})(V_{\mathrm{ext}}(\underline{r}) + \tfrac{1}{2}V_{\mathrm{H}}(\underline{r})) + E_{\mathrm{xc}}[n(\underline{r})]. \quad (1)$$

The expressions given here are referring to the non-spin-polarized case, but generalization is straightforward; V_{H} denotes the Coulomb potential of the electrons and V_{ext} the external potential, including the interaction with the ions. While the existence of the functional itself is proven, an exact formulation of the exchange–correlation part E_{xc} is unknown. Nevertheless, working approximations have been proposed on the basis of the homogeneous electron gas, which have contributed to the overwhelming success of this method in the past decades. In practice, the problem described by equation (1) can be expressed by a set of eigenvalue equations, which formally resemble the Schrödinger equation but act on single-particle wavefunctions. The Kohn–Sham equations are solved iteratively in a self-consistency approach, as the electronic density re-enters the potential of the Hamiltonian.

Our calculations were carried out using the Vienna *ab initio* simulation package (VASP) [38], which expands the wavefunctions of the valence electrons in a plane wave basis set. The interaction with the nuclei and the core electrons is described within the projector augmented wave (PAW) approach [39] yielding an excellent compromise between speed and accuracy (for an overview on the current state of the code and a review of recent applications, see [40]). For the accurate description of structural properties of ferrous alloys, the use of the generalized gradient approximation (GGA) for the representation of the exchange–correlation functional is mandatory. For the metallic nanoparticles, the formulation of Perdew and Wang [41, 42] in connection with the spin interpolation formula of Vosko, Wilk and Nusair [43] was used. Since the objects under consideration are zero dimensional and thus non-periodic, k-space sampling was restricted to the Γ-point. The description of the electronic properties with a plane wave basis requires a periodic set-up, thus the clusters were placed in a cubic supercell, with a sufficient amount of vacuum separating the periodic images. The supercells for the smaller systems were cubic, with a typical edge length of 22 Å, 28 Å and 32 Å for systems containing 147, 309 and 561 atoms, respectively, warranting a separation of about 9 Å of the periodic images. In order to check the convergence of the results with the supercell size, selected $N = 561$ clusters were studied within a 35 Å supercell, leading to an overall change of the absolute energy per atom of about 0.1 meV/atom. The effect on the energy difference between the clusters, was of one order of magnitude smaller. The clusters with $N = 923$ were placed in a unit cell with fcc basis vectors (lattice constant: 38.1 Å). This provides a more efficient use of resources as it allows a smaller volume of

the simulation cell, while maintaining sufficient separation of the periodic images. A cut-off for the plane wave energy of 268 eV was used for the ferrous systems. Gaussian finite temperature smearing with $\sigma = 50$ meV was used to speed up convergence. For the isomers with competitive energies, σ was reduced to $\sigma = 10$ meV in a second step. The $3d^6 4s^1$, $3d^7 4s^1$, $3d^8 4s^1$ electrons were treated as valence for Mn, Fe, Co and $3d^9 4s^1$ for Pt, respectively. In most of the calculations, the symmetrization of wavefunctions and forces was switched off, allowing for symmetry-lifting changes of the structure. The geometrical optimizations were carried out on the Born–Oppenheimer surface using the conjugate gradient method. The structural relaxations were stopped when the energy difference between two consecutive relaxations was less than 0.1 meV, leading to a convergence of forces down to the order of 10 meV Å^{-1}.

Dynamical properties of bulk crystals such as phonon dispersions can be obtained from electronic structure calculations either by perturbation theory or by directly determining the force constant matrix. Within the harmonic approximation, the contributions of lattice vibrations to the Hamiltonian are given by

$$\mathcal{H}_{\text{phonon}} = \sum_{\alpha} \frac{\underline{p}_{\alpha}^2}{2M_{\alpha}} + \sum_{\alpha,\beta} \underline{u}_{\alpha} \underline{\underline{\Phi}}(\underline{R}_{\alpha} - \underline{R}_{\beta})\, \underline{u}_{\beta} + \cdots. \quad (2)$$

The first term refers to the kinetic energy of the ions, while the $\underline{u}$ in the second term describe the displacements of the ions α and β from their equilibrium positions, coupled by the force constant matrix $\underline{\underline{\Phi}}$. The latter can be determined from the force acting on ion α after displacement of ion β:

$$\underline{F}_{\alpha} = -\frac{\mathrm{d}E}{\mathrm{d}\underline{u}_{\alpha}} = -\sum_{\underline{L}} \sum_{\beta} \underline{\underline{\Phi}}(\underline{R}_{\alpha} - \underline{R}_{\beta} + \underline{L})\, \underline{u}_{\beta}. \quad (3)$$

In highly symmetric systems only a few displacements are necessary to completely determine $\underline{\underline{\Phi}}$. The summation over the distance vectors $\underline{L}$ takes care of the fact that the infinite crystal is represented by periodic repetition of finite supercells separated by $\underline{L}$. Fourier transformation of the force constant matrix yields the dynamical matrix:

$$D^{\alpha\beta}(\underline{q}) = \frac{1}{\sqrt{M_{\alpha} M_{\beta}}} \sum_{\underline{L}} \Phi^{\alpha\beta}(\underline{R}_{\alpha} - \underline{R}_{\beta} + \underline{L})\, \mathrm{e}^{\mathrm{i}\underline{q}(\underline{R}_{\alpha} - \underline{R}_{\beta} + \underline{L})}. \quad (4)$$

The squares of the phonon frequencies $\omega(\underline{q})$ are now given by the eigenvalues of the dynamical matrix. For the Fourier transform, the summation over $\underline{L}$ is usually omitted for practical reasons, so that the final result is only exact for wavevectors $\underline{q}$ that are commensurate with the supercell. A simple but in many cases sufficient procedure to determine finite temperature properties is the quasiharmonic approximation. The (properly normalized) phonon density of states $g(\omega, V)$ obtained from ground state phonon calculations at different volumes can be used to obtain an approximation of the free energy at finite temperatures:

$$F(V,T) = -k_{\text{B}} T\, \ln(\mathcal{Z}_{\text{Phonon}}) = \int \mathrm{d}\omega\, g(\omega, V) \left(\frac{\hbar\omega}{2} + k_{\text{B}} T\, \ln(1 - \mathrm{e}^{-\hbar\omega/k_{\text{B}}T}) \right). \quad (5)$$

It should be noted that the entropy contributions derive solely from the changes in $g(\omega, V)$ at different volumes; many particle contributions such as phonon–phonon interactions are not included. To calculate temperature induced changes of the phonon dispersions from first principles, more expensive methods such as the self-consistent phonon renormalization proposed by Souvatzis [37] must be employed.

The phonon dispersions in section 5 have been obtained within the direct force-constant approach using the PHONON package by Krzysztof Parlinski [44]. By this, an orthorhombic supercell was constructed consisting of 40 atoms formed by five tetragonal unit cells stacked in the [110] direction. This corresponds to the direction along which the phonon softening of the TA_2 branch is found in experiment. The dynamical matrix is constructed from the Hellmann–Feynman forces obtained by *ab initio* calculations from specific displacements of the atoms in the supercell using the VASP code. For the $1 \times 5 \times 1$ supercell the mesh for the integration in reciprocal space was set to $10 \times 2 \times 8$ Monkhorst–Pack grid points. All phonon dispersions were calculated for the volume corresponding to the equilibrium lattice constant at zero magnetic field and zero temperature, $a_0 = 5.8067$ Å. We used pseudopotentials with $3d^9 4s^1$ as valence for Ni, $3d^6 4s^1$ for Mn and $4s^2 4p^1$ for Ga and a cut-off energy $E_{\text{cut}} = 353$ eV. For the simulation of the twin boundary motion processes, k-point sampling was restricted to the Γ-point only as a consequence of the large simulation cell. The plane wave cut-off was set to 337 eV and the exchange–correlation potential in the formulation of Perdew, Burke and Ernzerhoff [45] was used. Again, the geometric relaxations performed using the conjugate gradient method were carried out until the difference between total energies of two consecutive steps fell below 0.1 meV.

Parallelization is implemented in the VASP code using calls to the message passing interface (MPI) library. Parallel linear algebra routines (e.g. eigensolver) are used from the ScaLAPACK library. The installation on the IBM Blue Gene did not require major changes in the code. The peculiarity of the IBM Blue Gene/L concept is the huge packing density, which allows 1024 double-processor (700 MHz PowerPC 440d) nodes with a peak performance of 5.6 GFlop s^{-1} to be placed into one rack (for an overview, see [46]). Its successor, the Blue Gene/P, provides 4096 cores per rack (850 MHz PowerPC 450d), where four cores make up one node. To allow sufficient air cooling, power consumption was kept low by reducing the clock frequency of the CPUs and providing only a limited amount of main memory, 512 MB per node (2 GB for the Blue Gene/P)[1]. The Blue Gene/L hardware allows the memory to be divided between both CPUs ('virtual node' mode) or to be dedicated to one processor alone, while the other takes care of the communication requests ('communication coprocessor' mode), while the Blue Gene/P provides for each node true fourfold symmetrical multiprocessing on request. To increase scalability, a threefold high-bandwidth, low-latency network is implemented. In fact, the quality of the high-speed interconnect plays a decisive

[1] The numbers for the main memory provided here apply to the Blue Gene installations at Forschungszentrum Jülich, configurations with twice the memory are available from IBM.

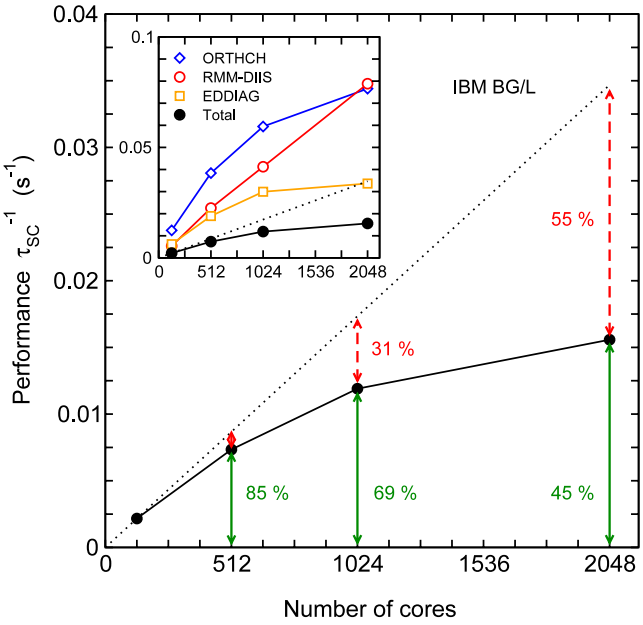

Figure 3. Scaling behaviour of a nanocluster with 561 Fe atoms on the IBM Blue Gene/L obtained with the VASP code. The performance given by the inverse average computation time for an electronic self-consistency step, τ_{SC}^{-1}, is shown as a function of the number of cores (black circles). The dashed lines describe the ideal scaling behaviour. The inset shows a double logarithmic plot of τ_{SC}. The open symbols in the inset refer to the scaling of the most time consuming subroutines (originally published in [25]).

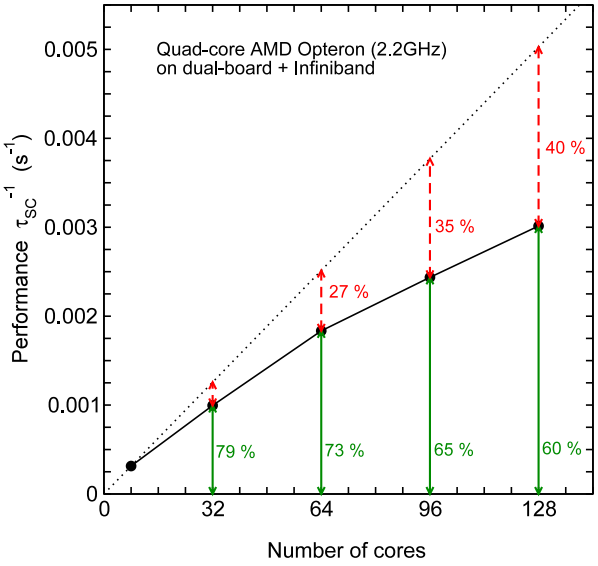

Figure 4. Scaling behaviour of a nanocluster with $Fe_{265}Pt_{296}$ (561 atoms) on a contemporary PC cluster (eight boards with 2×2.2 GHz quad-core Opteron processors and InfiniBand interconnect). The performance data were obtained with the same code in the same fashion as for the Blue Gene/L (cf figure 3).

role for the successful usage of the DFT code on a massively parallel system, which is demonstrated by scaling benchmarks in figures 3 and 4.

Although DFT calculations are generally considered to be demanding with respect to memory and I/O bandwidth, we can show that large systems can be handled efficiently on the Blue Gene despite its severe restrictions concerning operating system, partitioning and main memory per node. So far, systems of up to 923 spin polarized transition metal atoms, corresponding to 8350 valence electrons, have been successfully treated on the Blue Gene/P including geometric optimizations; for a larger test system with $N = 1415$ atoms ($Fe_{679}Pt_{736}$ nanocluster with 12 792 valence electrons) it was at least possible to reach electronic self-consistency. Figure 3 demonstrates that the VASP code can achieve 69% of the ideal performance on 1024 processors of the Blue Gene/L for a Fe_{561} cluster; in this case, the coprocessor mode was used to make use of the full memory per node on one processor. In particular, the optimization of the trial wavefunctions according to the residual vector minimization scheme (labelled 'RMM-DIIS' in figure 3) scales nearly perfectly, even at the largest processor numbers under consideration. However, with increasing number of processors, its computation time is outweighed by other routines ('EDDIAG' and 'ORTCH') providing the calculation of the electronic eigenvalues, subspace diagonalization and orthonormalization of the wavefunctions, making use of linear algebra routines from the ScaLAPACK library and performing fast Fourier transforms. The scaling of these routines may become the primary obstacle when attempting to run the VASP code on $\mathcal{O}(10^4)$ processors as provided by next-generation supercomputers.

A comparable benchmark of the VASP code on contemporary off-the-shelf PC hardware, however, led to a rather disillusioning result (figure 4). Despite extensive tuning, acceptable scaling was achieved only with up to 100 cores. This demonstrates that it is not necessarily the code which should be made responsible for a dissatisfying parallel performance. When attempting to touch the current limits, special care must be taken in the selection of the appropriate computer hardware, too.

3. Structure and magnetism of elemental nanoclusters

Although elemental 3d transition metal nanoclusters—in contrast to binary or multimetallic systems—hardly fulfil the criteria for functional magnetic materials even in the widest sense, we will devote our first section to this topic as structure and magnetism may be delicately related even in these seemingly simple systems (for recent reviews in this field, see, e.g., [47–50]). Elemental nanoparticles have raised much attention since they allow, e.g. in gas phase experiments, the direct observation of the crossover from bulk to atomic properties, circumventing the two- and one-dimensional (surface and chain) cases, which require substrates to stabilize the low dimensional structures experimentally. Prominent examples are the crossover behaviour of magnetic moments observed in 3d transition metal nanoclusters as a function of the cluster size, which was studied in the seminal experiments of Billas *et al* [51–53], or the discovery of significant magnetic moments in small gold nanoparticles or

clusters of 4d and 5d transition metals such as Rh, Pd, or Pt, which are non-magnetic in their bulk phases. Not only magnetism, but also the structure of small nanoparticles, is strongly affected by the increased surface-to-volume ratio at smaller sizes. This leads to a competition between surface energies and contributions arising from the core structure and internal interfaces and consequently to a crossover between different structural motifs as a function of the cluster size. This has been extensively studied and understood in the framework of simple model systems such as Lennard-Jones clusters [54–57], which can be easily handled in the framework of classical molecular dynamics and also with empirical model potentials [48, 58]. Here, multiply twinned icosahedral and decahedral structures are favoured at smaller sizes, while single crystalline morphologies prevail for larger sizes. A simple motivation can be given on the basis of a phenomenological third order polynomial law, expressing the binding energy as a function of the lateral system dimension, i.e. the third root of the system size N (e.g. [48]):

$$E(N) = aN + bN^{2/3} + cN^{1/3} + d. \tag{6}$$

Here, a, b, c, and d describe the contributions to the binding energy arising from the particle volume, the facets, the edges, and the vertices, respectively. These coefficients depend on the material itself, but also on the shape of the particle. With decreasing system size, the terms located on the right become increasingly important and it is straightforward to conceive that a multiply twinned morphology with higher coordinated surfaces and thus lower surface energy such as the icosahedron may become competitive with single-crystalline isomers which lack the adverse contributions due the appearance internal interfaces and strain in the volume part. Another example where classical schemes provide fundamental insight into particle shape and formation is simulations of closed-shell non-magnetic Al clusters in the truncated octahedron structures showing superheating behaviour with respect to the bulk melting temperature and coexistence of melting and non-melting surfaces [59].

Heavier elements such as Au and Pt furthermore form planar or even amorphous structures at smaller cluster sizes. Especially for these elements, but also for systems which are expected close to magnetic or magneto-structural instabilities, it may be doubted whether classical molecular dynamics based on empirical pair potentials—despite their undeniable merits in cases like the above mentioned—can give a reliable account of structural properties without benchmarks against parameter-free first-principles calculations. Due to the large computational demands, most of the *ab initio* investigations have been performed for small systems with around 50 atoms or less or without structural optimizations (see, e.g., [60–64] for the case of iron clusters or [65, 66] for a comprehensive investigation of small Ni-group clusters). Nevertheless, a couple of early exceptions exist, e.g. for Pd_{147} [67] and Sr_{147} [68]. Calculations of Pd isomers with size $N = 309$ in an icosahedral and octahedral symmetry have also been reported using the Turbomol package [69]. Recently, a report on the size dependence of magnetism in unrelaxed Fe clusters of up to 400 atoms has been published [70], reproducing the experimental results in the considered size range, as was also found previously from semi-empirical (tight-binding) calculations [71, 72]. It should be noted at this point that the size dependence of magnetic moments in the late 3d transition metal clusters is usually not well described by simple phenomenological expressions separating the core contribution, μ_{bulk}, and the surface contribution, μ_{surface}, to the magnetic moment, which is expected to hold in the limit of large cluster sizes N:

$$\bar{\mu}_{\mathrm{cluster}}(N) = \mu_{\mathrm{bulk}} + (\mu_{\mathrm{surface}} - \mu_{\mathrm{bulk}})N^{-1/3}. \tag{7}$$

Especially in the case of iron, more elaborate models of bcc clusters, taking into account details of the atomic cluster structures, as the variation in the coordination number of the surface atoms due to, e.g., partially filled geometric shells, cannot reproduce the experimental trend properly either [47, 74, 75]. The strong deviations from the experimental findings were confirmed by a later *ab initio* study covering structurally optimized Fe clusters with sizes of up to 641 atoms [73]. Xie and Blackman [76, 77] argued that the neglect of the magnetocrystalline anisotropy of the clusters which provides a coupling of magnetism to the rotational degrees of freedom can lead to a significant underestimation of the moments in the analysis of the time of flight experiments and may thus account for the observed behaviour. Our investigations, on the other hand, give evidence that the experimental trend may alternatively be related to the occurrence of a previously unreported shell-wise Mackay-transformed (SMT) modification at icosahedral magic cluster numbers. This structure is characterized by an icosahedral outer shape, bcc-like coordinated outer shells and a ferrimagnetic face centred cubic (fcc) cluster core [25, 73, 78], and is possibly kinetically stabilized during the gas phase growth process [79]. These finding can be well understood from the electronic structure, which is laid out in the following subsection in greater detail.

3.1. Structure and magnetism of iron clusters

Iron is certainly one of the most important materials of our time, not only as is it omnipresent as one of the central constituents of our planet but also due to its manifold applications, arising not least from its unusual allotropy. Iron possesses a complex structural phase diagram, with the body centred cubic (bcc) α- and δ-phases below 1185 K and above 1667 K, the face centred cubic (fcc) γ-phase in between and the hexagonal close packed (hcp) ϵ-phase at high pressures. In the fcc γ-phase a variety of competing magnetic states have been discovered, which were brought into connection with magneto-structural anomalies as the Invar effect and the magnetic shape memory behaviour in Fe-rich Fe–Ni, Fe–Pd and Fe–Pd alloys, where the fcc structure is also present at ambient conditions. Iron also provides a lot of interesting applications in the form of nanoparticles, especially in the field of biomedicine (for an overview, see, e.g., [80]).

The systematic scan of the potential energy surface in order to find the most stable morphologies is a demanding task even for small clusters containing a few to a few tens of

atoms [81]. But the numerical effort increases exponentially with the size and becomes hopeless in the nanometre range. Therefore, it is necessary to restrict the investigation to a subset of paradigmatic morphologies. As a consequence, so-called magic number clusters have evolved as the *Drosophila* of size dependent structural investigations in nanoparticle physics. Their size N is a function of the number n_s of closed geometric shells:

$$N_{\text{magic}} = 1/3(10n_s^3 + 15n_s^2 + 11n_s + 3) = 13, 55, 147, 309, 561, 923, 1415, \ldots. \quad (8)$$

Magic cluster sizes appear to be particularly stable for the late 3d elements [82], especially Ni and Co. Magic number clusters according to equation (8) allow for a comparison of several paradigmatic geometries: single crystalline cuboctahedra with face centred cubic (fcc) structure, perfect Mackay icosahedra [83] and Ino decahedra [84], i.e. pentagonal bi-pyramids with symmetrical truncations of their ten faces. Isomers with a body centred cubic (bcc) lattice, which are indispensable for ferrous systems, can be obtained from cuboctahedra by a Bain transformation [85].

In contrast to the ideal morphologies according to equation (8), the geometries observed in experiments often show modifications which reflect the competition between obtaining spherical shape and a favourable ratio between facets with different crystallographic orientations and different surface energies. Improved fcc isomers (e.g. truncated octahedra which follow a different formation law) can be obtained from a Wulff construction [86], according to which the most favourable truncated structure fulfils the following relationship between surface energies γ and the distances d of the facets from the centre of the cluster:

$$\gamma_{(100)}/\gamma_{(111)} = d_{(100)}/d_{(111)}. \quad (9)$$

As contributions from edges and vertices in equation (6) are neglected in this reasoning, the Wulff construction is expected to hold for larger sizes, but introduction of higher order faceting making the cluster shape more spherical may also lead to deviations in this case [48]. Also, Marks decahedra [87] with smaller truncations and re-entrant cuts at the edges are often found to be more favourable than Ino decahedra.

The optimized morphologies usually harbour a different number of atoms for each geometrical motif. For instance, single crystalline truncated octahedra (TOs) are given by the following construction law [88]:

$$N_{\text{TO}} = 1/3(2n_l^3 + n_l) - 2n_c^3 - 3n_c^2 - n_c. \quad (10)$$

These are characterized by two indices, the edge length of the complete octahedron, n_l, and the number of layers cut off at the respective vertices, n_c. Here, the conditions $n_l = 2n_c + 1$ and $n_s = n_c + 1$ yield perfect magic number cuboctahedra according to equation (8). For a quantitative prediction of the most likely surface truncations improving the relative stability, the surface energies γ of the competing facets needs to be known in detail. For multiply twinned morphologies, strain and twin boundary energies must also be taken into account (for a detailed discussion, see [89]):

$$E(N) = N\,(E_{\text{bulk}} + \Delta E_{\text{strain}}) + A_{\text{TB}}(N)\,\gamma_{\text{TB}} + \sum_{(hkl)} A_{(hkl)}(N)\,\gamma_{(hkl)}, \quad (11)$$

where E_{bulk} and ΔE_{strain} are the cohesive energy of a bulk atom of the respective crystal structure and the corresponding correction due to internal strain and A the respective (size dependent) areas of the twin boundaries (TB) or surfaces denoted by the respective indices. Again, contributions from edges and vertices are neglected. The accurate determination of surface and twin boundary energies is a methodologically and computationally demanding task, especially for the case of materials with a strong interdependence between structure and magnetism such as iron or in binary alloys. Magic cluster sizes, on the other hand, allow for the direct comparison of the most important structural motifs and are thus at least good for drawing a coarser, more qualitative picture.

Until recently, the structural evolution of iron clusters as a function of particle size had not been resolved: transmission electron micrographs (TEMs) of 6 nm particles suggest a bcc structure [91], while for 13 atoms first-principles calculations predict a Jahn–Teller distorted icosahedron [92, 93]. For the next closed-shell magical number, i.e. 55 atoms, a previously unreported morphology was found to provide a good candidate for the ground state [73, 79]. Based on this discovery, the concept of the so-called shell-wise Mackay-transformed (SMT) morphologies was introduced by Georg Rollmann and Alfred Hucht, which will be explained in more detail below.

On a larger size scale, estimations of the energetic order between the different paradigmatic cluster morphologies were only available from structure optimizations with classical empirical potentials [94], predicting a crossover between icosahedral and bcc morphologies at sizes around 2000 atoms, while the binding energies were reported to be comparatively close for these morphologies. Keeping in mind that these calculations largely neglect the influence of magnetism on structure, which is especially important in the case of iron, this result can hardly be considered conclusive. A detailed analysis based on first-principles electronic structure methods was thus launched by us to settle this fundamental question [73]. The investigation comprised icosahedral, cuboctahedral and bcc (Bain-transformed cuboctahedra) clusters with up to five completed geometrical shells according to equation (8), i.e. $N = 561$ atoms corresponding to, approximately, 2.5 nm diameter. In addition, more spherical bcc geometries were considered with non-magic sizes up to $N = 641$ atoms. Technically, the calculations were carried out using the VASP code in the fashion described in the preceding section, including unconstrained geometric optimizations on the Born–Oppenheimer surface. The total energies resulting for different geometries as a function of the number of closed geometric shells displayed in figure 5 reveal that for three closed shells (147 atoms) and larger the bcc isomer marks the lowest energy conformation, especially in comparison to (high symmetry) icosahedral and the cuboctahedral isomers, which rapidly approach with increasing n the energy difference between the

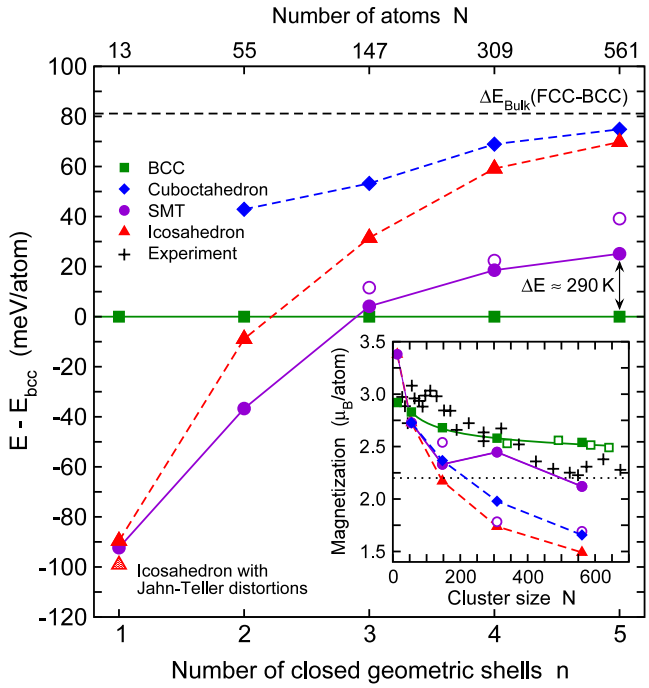

Figure 5. Comparison of the energies of various isomers of elemental iron nanoclusters as a function of the number of closed geometric shells n (data originally published in [73]). The bcc isomer has been chosen as reference and thus represents the abscissa. Open circles denote SMT isomers with alternative magnetic configurations which are not lowest in energy. The lines are intended as guides to the eye; broken lines refer to unstable structures. The horizontal dashed line marks the bulk value for the fcc–bcc energy difference [90]. The inset shows the variation of the average magnetic moment of the different isomers as a function of the cluster size (experimental moments taken from [52]). Open squares represent non-magic-number bcc isomers. The solid line connecting the bcc values is a fit to equation (7).

bcc and fcc phases obtained by bulk *ab initio* calculations [90]. An extensive comparison between the total energies of a larger number of unrelaxed geometries at intermediate sizes obtained with the PARSEC [95] real space DFT method suggests that bcc isomers already supersede icosahedral and fcc motifs below $N = 100$ [70, 73]. The average magnetic moments obtained by both approaches agree well for the bcc case, while for cuboctahedra and icosahedra the fully optimized structures rather exhibit an onion-type ferrimagnetic ordering of the closed geometric shells, reducing the average moment considerably, as shown in the inset of figure 5. The magnetic ordering of Fe cuboctahedra as a function of the lattice spacing has been investigated recently in more detail [96, 97]. Compared with the experimental data of Billas *et al* [51, 52], the theoretical data follow the experimental trend up to sizes of $N = 400$ atoms but deviate significantly beyond. This also applies for magic number clusters as well as for more compact bcc clusters up to $N = 641$ atoms, which possess an improved surface-to-volume ratio as compared to the Bain-transformed cuboctahedra, and is in accordance with previous results obtained by other approaches [47].

For all sizes, cuboctahedral and icosahedral shapes are maintained during the optimization procedure, if the atoms are strictly kept in their symmetric positions and eventually additional symmetry constraints for charge densities and forces are imposed. Already small distortions along the Mackay path [83], however, are sufficient to induce a transformation, which finally leads to the above mentioned shell-wise Mackay-transformed conformation. The SMT state is very robust and can be obtained from different initial configurations [98], and has recently also been reproduced by classical molecular dynamics simulations with empirical EAM potentials [99] for clusters with up to 15 closed geometric shells [100].

The Mackay path is analogous to the Bain path [85], which connects fcc and bcc bulk phases by changing the extension of the c-axis with respect to the equal a and b axes of the crystal, a diffusionless, displacive mechanism relating the cuboctahedron with a single crystalline fcc structure to the non-crystallographic icosahedron. During this process 12 pairwise adjacent triangular (111) faces of the icosahedron stretch along their common edge and turn into the same plane to form the six square (100) faces of the cuboctahedron. An illustration of this process is given in figure 7 for the case of the $N = 561$ isomers. The original Mackay process affects all shells simultaneously. Such homogeneous transformations have been recently studied in detail for magic number Pb clusters of different sizes with *ab initio* methods [101]. In the SMT isomers, however, the degree of transformation varies gradually from shell to shell, from a perfect cuboctahedron in the particle core, to a nearly icosahedral shape of the surface shell. This is slightly distorted by the inward bending of the common edge between the two triangular facets which correspond to the square face of the cuboctahedron. The SMT represents the lowest energy isomer for $n = 2$ and is only slightly higher in energy than the Jahn–Teller distorted icosahedron with only one closed shell for $N = 13$. For $n \geqslant 3$, however, the bcc isomers form the ground state. Nevertheless, the energy of the SMT is greatly reduced compared to the symmetric icosahedra and cuboctahedra and still in the range of thermal energies to the bcc isomer for $N = 561$. Also the magnetic structure differs: while still being ferrimagnetic with an onion-type (shell-wise) alternating arrangement of layers in the particle core, the average moment of the SMT is systematically larger than the moment of icosahedra and cuboctahedra: for the SMT the outermost three shells are ferromagnetically aligned (cf figure 6), while for the latter only surface and subsurface shells have the same magnetization direction. Due to its ferrimagnetic spin structure, the average moment of the SMT isomer is considerably smaller than the average bcc moment and agrees therefore much better with the experimental data. It is certainly too speculative to conclude from this evidence that the occurrence of SMT isomers around $N = 561$ explains the dip in the cluster moments in the experiments of Billas *et al*, but it should be kept in mind that icosahedral features are frequently observed in many materials during solidification from the melt or during gas phase synthesis [102]. Also, from recent DFT calculations, icosahedral or, respectively, SMT growth has been proposed as a likely growth mode for small Fe clusters from the gas phase [79].

The search for the origin of this unusual transformation requires a more detailed structural analysis. For several

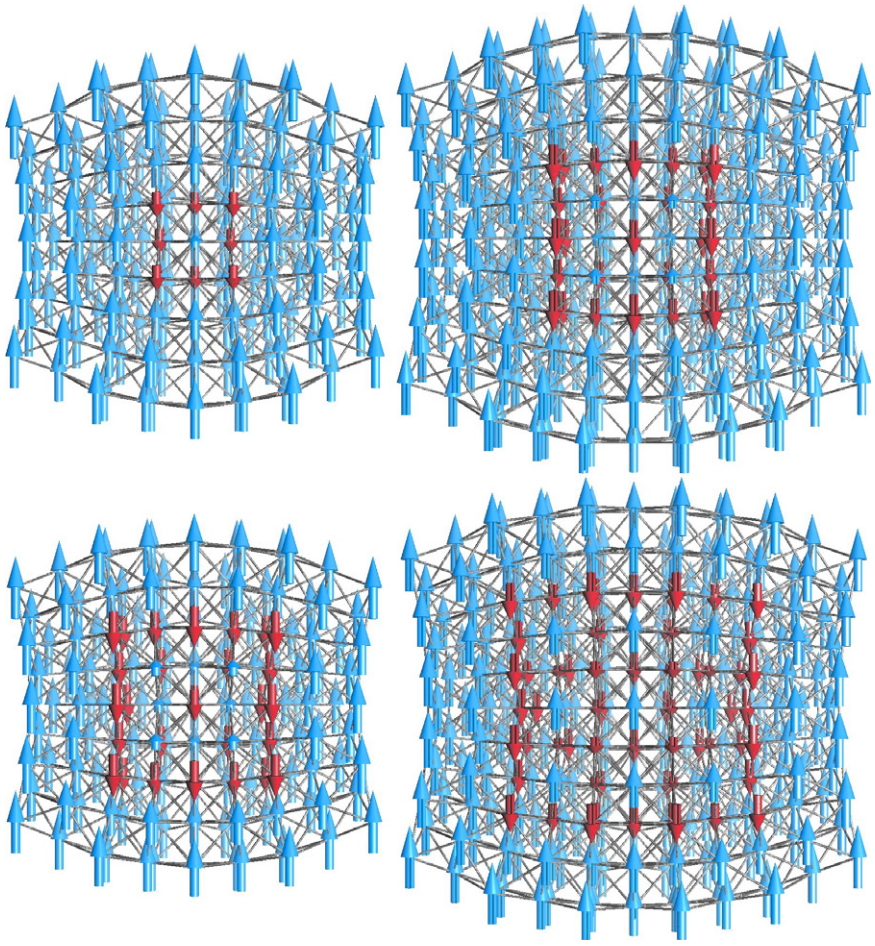

Figure 6. Ferrimagnetic spin configurations of the Fe_{309} (left) and Fe_{561} (right) SMT isomers ($n = 4$ and 5, respectively) shown as cross-sections. The arrows refer in length and orientation to the atomic moments. The upper isomers correspond to the high-moment structures with the lowest energy. The isomers at the bottom correspond to low magnetization structures marked by the open circles in figure 5.

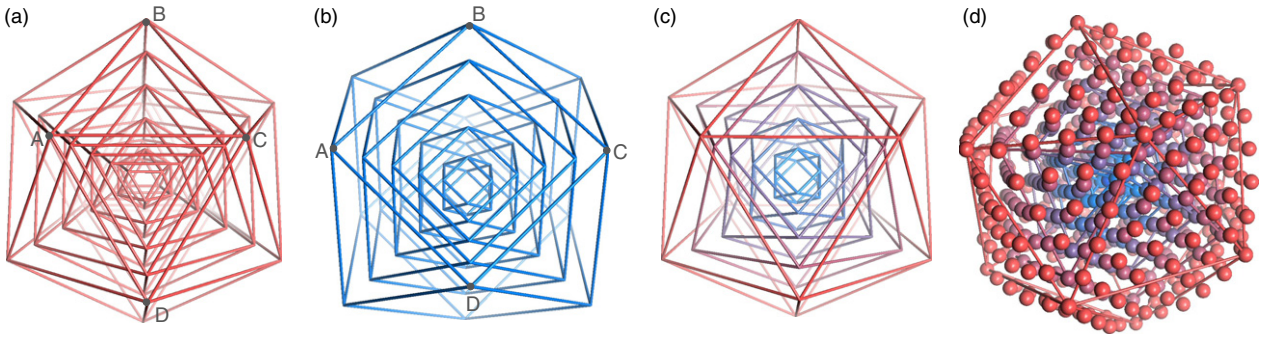

Figure 7. Edge models of the optimized Fe_{561} icosahedron (a), cuboctahedron (b) and SMT isomer (c). Separately for each shell, the corner atoms of the faces are connected by lines; the atoms themselves are omitted for clarity. The complete SMT isomer including all atomic positions is shown in (d). For icosahedra and cuboctahedra, shells of the same shape but different sizes are stacked into each other. For the SMT isomer, the shape of the outermost shell is icosahedral and continuously changes towards the inside along the Mackay path to a cuboctahedron, which represents the shape of the innermost shell, which is reflected by the gradual change of colour from red to blue in (c) and (d). The Mackay transformation works by stretching the bond $\overline{AC}$ of the icosahedron and turning the two adjacent triangular faces ABC and ACD into the same plane, producing the square face ABCD of the cuboctahedron. Illustrations are partially taken from [78].

hundred atoms, the inspection of the structural environment at the atomistic level may, however, become a tedious and fallible task without appropriate statistical means. A well corroborated approach has been developed in the classical molecular dynamics community where the classification of structural transformations in large systems is a common request. The so-called common neighbour analysis (CNA) [103, 104] allows a comprehensive comparison of the SMT structure with other morphologies. If we restrict ourselves to the first (for bcc up to the second) neighbour shell, a set of three-index signatures

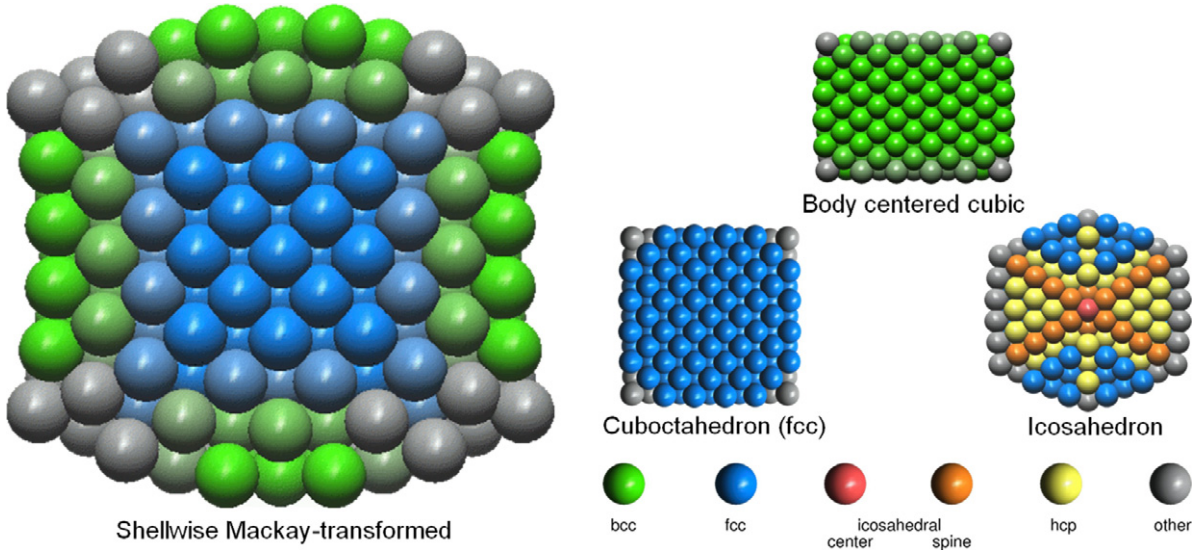

Figure 8. Cross-sections of optimized geometries of 561-atom iron nanoparticles. The colour coding describes the local coordination of the atoms obtained by a common neighbour analysis. Bright colours refer to perfect matching of the CNA signature with the ideal bulk and surface configurations. With increasing number of deviations the colours turn to grey. Adapted from [25].

provides a classification of the local structural environments of the atoms in the cluster. The indices refer—in the respective order—to the number of nearest neighbours both atoms have in common, the number of bonds between these neighbours, and the longest chain of bonds connecting them. Each ideal bulk structure is characterized by a specific set of 12–14 individual signatures. For surface and subsurface atoms different signatures apply. A comparison of the CNA of atoms of the SMT with the respective positions in the other, ideal isomers can now attribute to each atom a specific characterization of the local environment. Figure 8 shows the result of a CNA applied to the optimized isomers, the colours indicating the local structural environment. In many cases, the coincidence is not perfect and a few signatures differ with respect to the ideal cases. Here, the colours turn to grey, which marks an unidentified environment, with an increasing number of non-matching signatures. While the bcc and fcc clusters are uniform in structure, we find for the icosahedron the typical mixture of fcc, hcp and—along the fivefold symmetry axes—icosahedral environments. The SMT isomer, however, shows a rather unexpected pattern: while the central atoms are fcc coordinated according to the nearly completed Mackay transformation of these shells, we find no trace of the typical icosahedral signatures in the outermost shells, which, however, retain their overall icosahedral shape. Instead, their signatures show typical signs of the energetically favourable bcc-like coordination, suggesting that the tendency of bulk Fe to form a bcc lattice at low temperatures is also responsible for the stabilization of SMT structures in nanoparticles. In this case bcc-specific features should also show up in the electronic density of states (DOS).

A comparison of the DOS for different $N = 561$ morphologies is presented in figure 9. For the bcc isomer, the site resolved DOSs of the core and subsurface atoms exhibit the typical valley in the centre of the d band—a characteristic feature for bulk bcc alloys. While the majority d band is nearly filled, the Fermi level locks into this valley in the minority channel, providing a motivating argument for the extraordinary stability of the ferromagnetic α-phase of bulk iron (see the book of Kübler [105] for a detailed discussion). In fact, the contributions of subsurface and surface shells bear strong similarities to the bcc case, while the contributions of the core atoms with their ferrimagnetic alignment rather resemble the result for the cuboctahedral or icosahedral morphologies.

While the density of states can in principle be detected by photoemission experiments, the particular examples provided in figure 9 may—except for the case of the bcc cluster—not provide sufficiently distinctive features to discriminate between the structural motifs. An experimentally accessible quantity, which is directly related to the structure, is the pair distribution function (PDF). The inhomogeneous structural environment of the SMT results in a PDF which is qualitatively different from the other morphologies (figure 10). It does not compare well either to a linear combination of fcc and bcc PDFs, as could have been guessed from the CNA results, but rather to the experimental results of Ichikawa *et al* [106] obtained from a thin film produced by low-temperature condensation of evaporated iron. These exhibit features which are typical for amorphous alloys and were thus interpreted in this sense. Other related experiments are based on a sonochemical approach [107].

It has to be noted at this point that, while the existence of certain amorphous Fe-based alloys is well established in the literature (see, e.g., [108] and references therein), the possibility of amorphous pure iron is highly debated. While the SMT isomer is not amorphous in a literal sense, the transformation may be compared to the rosette-like structural excitations which were recently discussed as an amorphization mechanism for Pt and Au nanoclusters [109]. Recently, an intermediate amorphous-like phase was reported from empirical molecular dynamics simulations of 2.5 nm $Fe_{80}Ni_{20}$

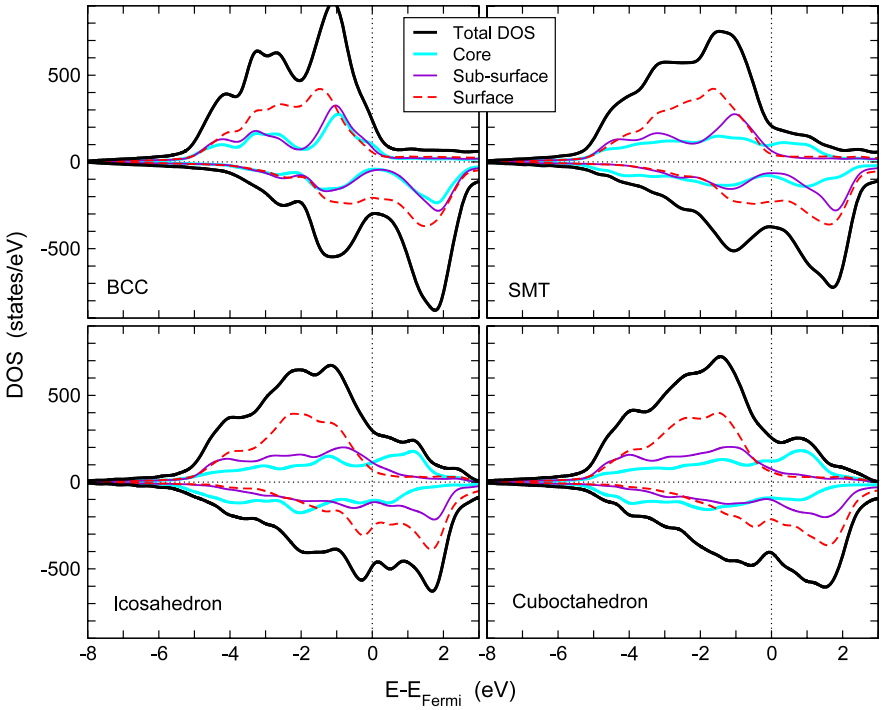

Figure 9. Total electronic density of states of the four Fe_{561} morphologies (thick black lines). Positive densities refer to the majority spin states, negative to the minority spin channel. The other lines mark the shell resolved element-specific contributions. Thick bright (blue) lines denote the DOS of the innermost three shells (147 atoms), thin dark (violet) lines the subsurface shell (162 atoms) and broken (red) lines refer to the surface shell (252 atoms). In order to concentrate on the essential features, the curves have been artificially broadened according to a Gaussian distribution with $\sigma = 0.2$ eV.

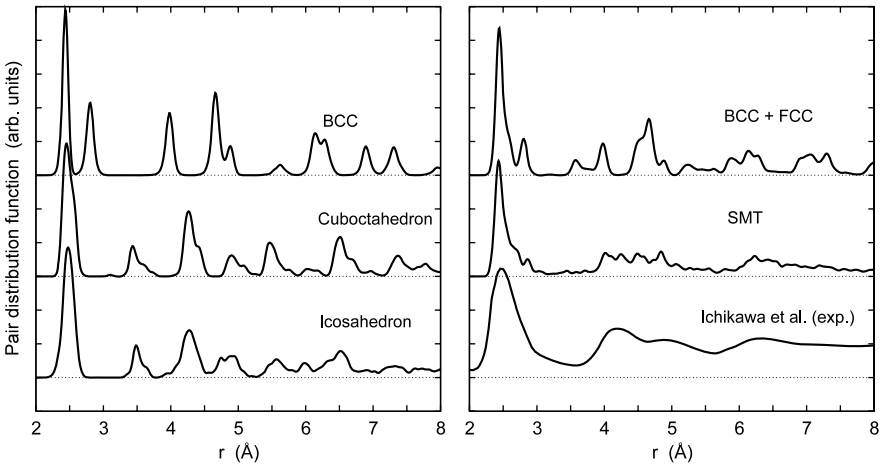

Figure 10. Pair distribution functions (PDFs) of the Fe_{561} isomers discussed in figure 8. For comparison a linear combination of the bcc and the cuboctahedral PDF (top right) as well as the experimental PDF (bottom right) of an Fe film produced by condensation of evaporated iron [106] is also shown (theoretical data partially from [78]).

clusters [110], which shows striking similarities concerning its PDF and other structural motifs such as the wave-like bending of atomic columns and planes, which is visible in figure 7. This can be seen as a further indication that SMT morphologies may in fact be realized in the experiment under certain environmental conditions.

3.2. Cobalt and nickel nanoparticles

Due to the multitude of different possible bulk phases with distinct magnetic properties, iron is certainly an exceptional case, also with respect to its properties on the nanoscale. For the other elements showing ferromagnetism in their bulk phases, a comparably rich behaviour is not expected. Figure 11 compares thus only the two most important magic number morphologies, icosahedra and cuboctahedra. For Ni and Co, icosahedra are strongly preferred over the whole size range, the energy difference being much larger as compared to Fe, especially in the case of Co. The magnetic properties (figure 12) approach the bulk values faster with increasing cluster size than is the case for iron, agreeing well with combined time-of-flight mass-spectroscopy and Stern–Gerlach

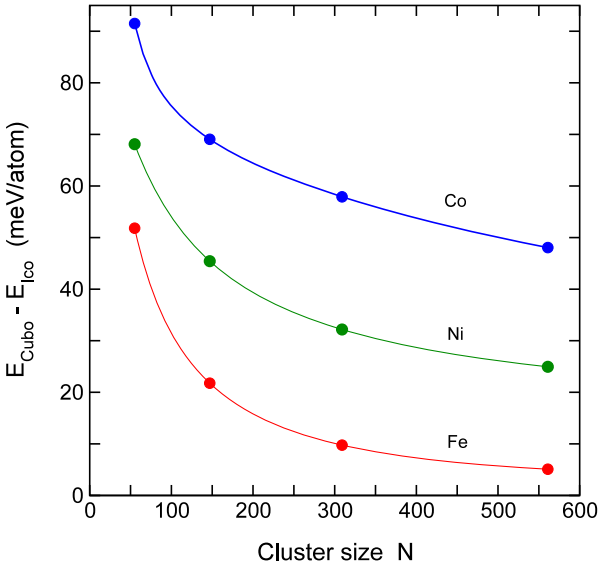

Figure 11. Energy difference between cuboctahedra and icosahedra of Co, Ni and Fe as a function of the cluster size. The lines are only guides to the eye.

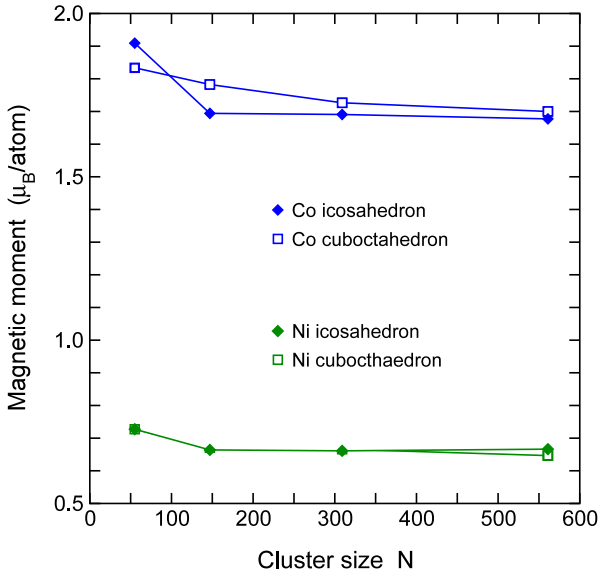

Figure 12. Size dependence of the averaged magnetic moment of Co and Ni clusters.

measurements [53] and the results of the extensive tight-binding studies of Xie and Blackman [15, 111, 112]. This makes these elements appear more suited for a successful description with empirical potentials. Especially for the case of Ni, the calculated energy differences between icosahedra and cuboctahedra coincide from $N = 147$ atoms upwards surprisingly well with the early results of Cleveland and Landman [58] based on empirical pair potentials.

From the electronic structure point of view, it is tempting to classify the preference for the icosahedral structure in terms of the electronic density of states. From figure 13 it becomes evident that the core and subsurface contributions do not differ significantly between the two morphologies of the same element and only slightly between the elements (except for the different exchange splittings). The most distinctive changes are visible with respect to the DOS of the surface atoms, suggesting that—in contrast to iron—the surface energy contributions play the dominant role in the determination of the particle shape.

4. Binary transition metal nanoparticles—in search of ultra-high-density magnetic recording materials

In the field of ultra-high-density magnetic recording (for an overview, see, e.g. [113]), there has been a long-lasting exponential increase in storage density over time: while about a decade ago, densities of 35 GBit/in^2 were state-of-the-art [7], the manufacturers nowadays face the TBit/in^2 scale. However, approaching this regime, development is slowing down [114] and it will be necessary to switch to new technologies to cross this line in order to finally reach densities of 10 TBit/in^2 or even beyond [115].

Magnetic data storage as in conventional hard disk drives currently relies on thin CoCrPtB microstructured magnetic films consisting of single crystalline grains with polydisperse size distribution. To average out the noise, the information has to be stored in the different magnetization directions of around 50–100 magnetically loosely coupled grains. The main obstacle to further miniaturization is presumably the so-called superparamagnetic limit, which threatens the long-time stability of the information stored. The Néel relaxation time τ of a macrospin with uniaxial anisotropy, representing the recording media grain, has an exponential dependence on the product of (uniaxial) anisotropy constant K_u and grain volume V divided by temperature T:

$$\tau = \tau_0 \exp\left(\frac{K_u V}{k_B T}\right). \tag{12}$$

This imposes a lower boundary for the possible size of a grain, which keeps its magnetization unaffected by thermal relaxation processes at room temperature for a sufficiently long period of time (usually decades). Today, two approaches beyond current technologies are discussed.

- Replacement of polycrystalline films by patterned media, where each bit is represented by a single thermally stable magnetic dot, which can be achieved using lithography techniques or by assemblies of nanoparticles. This reduces dramatically the area needed for one bit and also the interaction between neighbouring grains, but demands high standards with respect to monodispersity, magnetic properties and arrangement of the particles. Remarkable progress has been made in this field in the past years [5, 6, 116].
- Use of high anisotropy materials. This allows a reduction of the grain size stability limit inversely proportional to the increase in the anisotropy constant [7, 113]. Materials which are currently widely discussed in this respect are Fe–Pt and Co–Pt [117]. Several studies had suggested that particle sizes as small as 3 nm (for Fe–Pt, inferred from the bulk anisotropy constant) could be sufficient for

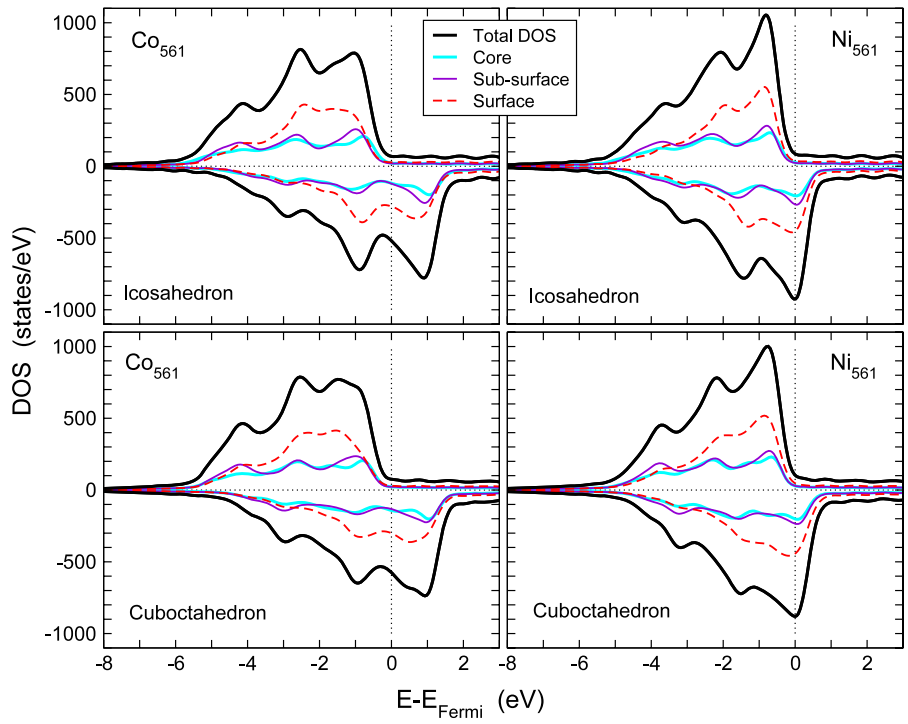

Figure 13. Electronic density of states of Co_{561} and Ni_{561} icosahedra and cuboctahedra. Lines have the same meaning as in figure 9.

Table 1. Collection of characteristic properties of contemporary and future storage media materials capable of storing information over a decade in grain sizes smaller than 10 nm (taken from [7]). Listed are uniaxial anisotropy K_u, coercive field H_C, and critical particle size D_p.

Alloy	K_u (10^7 erg cm^{-3})	H_C (kOe)	D_p (nm)
CoCrPtB	0.33	20	9.1
Co	0.45	6	8.0
FePd	1.8	33	5.0
FePt	6.6–10	116	≈3.0
CoPt	4.9	123	3.6
MnAl	1.7	69	5.1

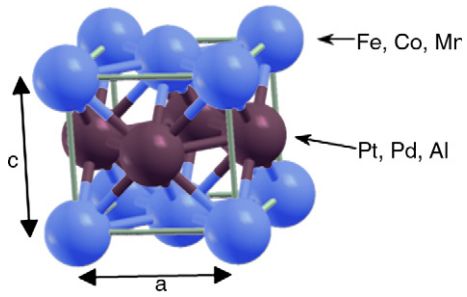

Figure 14. The $L1_0$ structure of FePt, FePd, CoPt and MnAl.

thermally stable storage of information [5, 118, 119] (for a comparison of several possible materials, see table 1).

Structural and magnetic properties of binary nanoparticles formed from the transition metal alloy Fe–Pt have been subject to a considerable number of investigations during the past years (for a recent overview, see, e.g., [120]). The stoichiometric $L1_0$-phase FePt, CoPt and FePd is characterized by a face centred tetragonal (fct) lattice with a layer-wise stacking of 3d and fourth and fifth row transition metals along the shortened axis (cf figure 14). The alternation of the elemental constituents gives rise to the unusually large magnetocrystalline anisotropy [121]—rather than the slight tetragonal distortion of a few per cent with respect to the fcc lattice parameters. Following [121], the comparison should be made with the cubic B2 structure, which then yields a rather large distortion with $c/a \approx 1.36$. Current production routes for Fe–Pt nanoparticles are to fabricate disordered fcc particles from gas phase experiments [122, 123] or wet-chemical production routes [5, 124, 125] and to obtain the ordered $L1_0$ phase in a further annealing step [6]. However, in recent times it was reported that $L1_0$ particles with a sufficient magnetocrystalline anisotropy may be difficult to obtain in the interesting size range [124, 126–129]. Recently, improved results have been reported after embedding the particles in a matrix, in micelles or by irradiating them with ions [130–132]. In most cases, however, compared to the coercivity of the bulk materials in table 1, the results obtained for small nanoparticles are rather disappointing from the magnetic storage point of view (see, e.g., [123]). Some of the experimental studies relate this to the incomplete order in these systems, as there is a critical particle size below which sufficient ordering cannot be achieved for thermodynamical reasons. Another possible explanation, which also accounts for larger particle sizes, is related to the appearance of $L1_0$ ordered domains with different orientations in the same particle, counteracting the development of one stable easy axis. Indeed,

high-resolution transmission electron microscopy (HRTEM) showed the occurrence of multiply twinned morphologies such as icosahedra and decahedra already at particle sizes around 6 nm [133–135] consisting of several strained twins (20 in the case of Mackay icosahedra and 5 in the case of decahedra). Therefore, such morphologies cannot be expected to exhibit a large uniaxial magnetocrystalline anisotropy, even if the individual twins are perfectly $L1_0$ ordered, because of their different crystallographic orientations.

As the crossover effects between different geometries at small particle sizes can be traced back to a competition between surface and core energies, two possible routes open up to suppress unwanted multiply twinned morphologies—either by changing the ratio of the surface energy of different faces, which can be effectively done by suitable ligands in wet-chemical approaches, or, on the other hand, by increasing the energy related to internal lattice defects, such as twin boundaries, which could be achieved, e.g., by alloying.

4.1. Fe–Pt and Co–Pt nanoparticles for data recording applications

In many elementary nanoparticles with fcc ground state in bulk, a competition between different morphologies is observed owing to the favourable (111) surfaces of the icosahedron, which gives the dominant energetic contribution at small particle sizes. In binary systems like Fe–Pt, segregation and ordering tendencies have to be considered, too. In this respect, we distinguish three different classes: disordered structures, ordered isomers and core–shell structures, corresponding to perfect surface segregation, with all Pt placed on the surface or in the shell below. The composition was fixed to the near-stoichiometric, perfectly $L1_0$ ordered cuboctahedra which are the most relevant isomers from the technological point of view. Although orbital magnetism is not explicitly included in our calculations, it is obvious from geometric considerations that the multiply twinned morphologies, even if the individual twins are $L1_0$ ordered, will not show the desired uniaxial magnetic anisotropy due to the multiple orientations of the twins in the nanoparticles. A deep understanding of the interplay between geometric structure, chemical ordering and magnetic properties will therefore be an important step towards the production of high anisotropy nanomaterials for ultra-high density magnetic data recording.

So far, most *ab initio* studies of binary transition metal clusters have been restricted to rather small sizes (for a recent review, see [81]). Thus, most theoretical investigations of Fe–Pt and Co–Pt nanoparticles have been carried out using continuum models [89], classical Monte Carlo and molecular dynamics simulations with empirical model potentials [136–143] or semi-empirical methods [144, 145]. The magnetism of spherical 2.5–5 nm $L1_0$ Fe–Pt nanoparticles embedded in a disordered alloy matrix has been investigated by means of the locally self-consistent multiple scattering (LSMS) method [146].

In order to shed more light on the origin of the experimental problems from the electronic structure point of view, we started *ab initio* calculations of Fe–Pt and Co–Pt nanoparticles with up to 923 atoms (≈3.0 nm in diameter), comparing more than 60 configurations of particles of both materials with different sizes [147–149]. Although the particles are too small to avoid superparamagnetism at room temperature, general trends can be formulated from the results, as the largest clusters already possess a balanced surface-to-volume ratio (45% at 2.5 nm and 32% at 4 nm).

The systematic investigation of binary alloy clusters raises more complications due to the additional compositional degree of freedom. Apart from the competition of various geometries, order–disorder and surface segregation effects must also be taken into account. Therefore, we must restrict ourselves, again, to a small number of paradigmatic morphologies. In addition, perfectly chemically ordered or segregated structures exist only for particular compositions and this usually depends on the particular distribution motif of the elements, such as a layered or shell-wise ordering or a perfect core–shell-like configuration. Comparing perfect motifs would require us to relate calculations for different compositions, which hampers the direct comparison of the relative stability of the isomers. In order to avoid these problems, we will chose one specific composition and most compositional motifs will consequently be approximated by randomly distributing the atoms of the excess species on the designated sites of the short element. As the central concern of our work is related to nanoparticles for ultra-high-density recording purposes, the stoichiometric $L1_0$ fct isomer with alternating Fe and Pt layers along the shortened c-axis is a distinguished case, since this is the closest approximant of the bulk alloy structure and thus expected to show the desired large magnetocrystalline anisotropy. Due to the symmetry of the structure, the two (001) surfaces of the $L1_0$ cuboctahedra have to be terminated by one species, either completely with iron or with platinum, respectively. This results in a slight off-stoichiometry, which decreases with increasing cluster size. For the Pt-rich case, the size dependence of the composition is given by the following relations:

$$\begin{aligned} N_{\mathrm{Fe}} &= \tfrac{1}{3}(5n^3 + 6n^2 + 4n) \\ &= 5, 24, 67, 144, 265, 440, \ldots, \\ N_{\mathrm{Pt}} &= \tfrac{1}{3}(5n^3 + 9n^2 + 7n + 3) \\ &= 8, 31, 80, 165, 296, 483, \ldots, \end{aligned} \tag{13}$$

where n is again the number of complete geometric shells. Exemplary *ab initio* calculations of $Fe_{265}Pt_{296}$ clusters [148] demonstrate that, in comparison to the perfectly $L1_0$ ordered Fe-covered isomer, a redistribution of the atoms in connection with covering the surface with Pt leads to a considerable gain in energy despite the imperfection of the order by placing the excess Fe on the Pt antisites. Therefore, in thermodynamic equilibrium, the Pt-terminated morphologies should dominate and we consequently focused on the isomers with predominately Pt-covered surfaces. This reasoning comes closest to the gas phase production route; for wet-chemical processes the kinetics of formation plays a much bigger role, which we currently cannot cover by *ab initio* simulations.

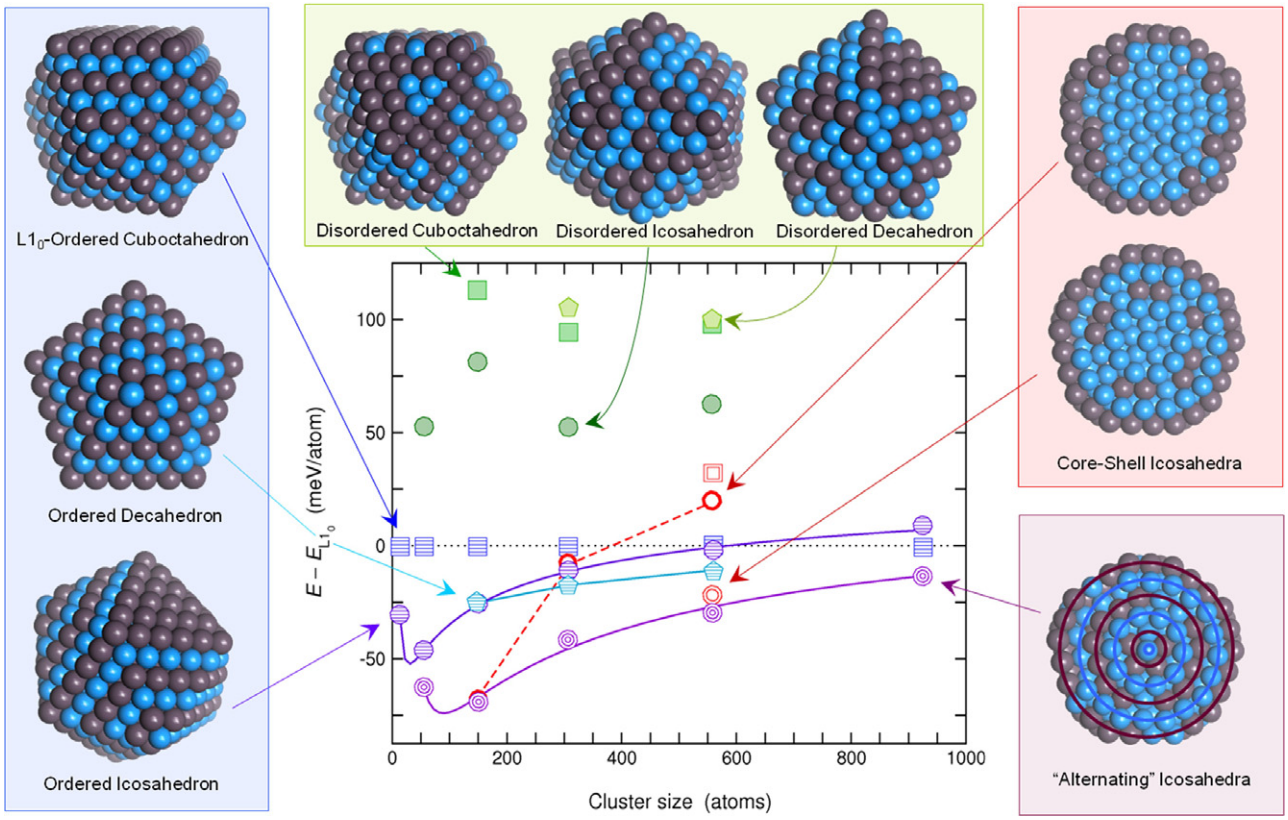

Figure 15. Morphologies of Fe–Pt nanoparticles and their corresponding energies as a function of the cluster size. The data up to $N = 561$ are taken from [147]. In the diagram, cuboctahedra are represented by squares, icosahedra by circles and decahedra by pentagons; the lines are guides to the eye. The energy reference is defined by the $L1_0$ cuboctahedron. Shaded (green) symbols denote disordered isomers, hatched (blue) symbols ordered structures, thick and nested symbols core–shell (red) icosahedra and cuboctahedra as well as icosahedra with shell-wise ordering tendencies (violet). Around the diagram, examples of the simulated cluster structures are shown. Only the structures with $N = 561$ atoms (265 Fe and 296 Pt) are depicted. Bright spheres (blue) refer to Fe atoms, dark spheres (brown) to Pt. The icosahedral core–shell structures on the right are shown as cross-sections, visualizing the inner arrangement of the atomic species. The circles drawn on top of the lowest energy icosahedron (right bottom) visualize the alternating, onion-type arrangement of Fe- and Pt-rich shells. The lines connecting the data points of ordered and alternating icosahedra represent polynomial fits to equation (6).

4.1.1. Size dependent properties of Fe–Pt nanoparticles. The investigated isomers are categorized in three major groups, ordered structures, disordered structures and core–shell motifs, which are symbolized by the (coloured) boxes in figure 15. The ordered morphologies (left, blue box) refer to the structures which reflect the strong tendency towards $L1_0$ ordering in bulk Fe–Pt. These comprise the $L1_0$ ordered cuboctahedron as the reference structure and an Ino decahedron with five individually $L1_0$ ordered twins and Pt-terminated (001) surfaces. The ordered icosahedron was obtained by applying a full transformation along the Mackay path [83] on the positions of the $L1_0$ cuboctahedron, while keeping the occupancy of the sites by the atomic species fixed, since this largely preserves the local chemical environment of the atoms. In fact, the multiply twinned ordered morphologies turn out to be lower in energy than the reference isomer, supporting the experimentally observed trends. This is especially significant for small clusters, with decreasing tendency towards larger sizes. For the ordered icosahedron a crossover to the single crystalline $L1_0$ morphology takes place around 600 atoms, which is in excellent agreement with the crossover size predicted on the basis of a continuum model according to equation (11) for a related icosahedron with 20 individually ordered $L1_0$ twins with random orientation of the c-axis [89]. It should be kept in mind that the nominal composition is varying with cluster size, which affects mainly the smallest investigated sizes.

For comparison, the three paradigmatic cluster shapes have also been studied as chemically disordered isomers (green centre box in figure 15). The icosahedral morphologies are again preferred over the decahedral and single crystalline structures, but all corresponding energies are considerably above the values of the ordered morphologies, which is expected due to the strong ordering tendencies in bulk Fe–Pt. In order to obtain a quantitative estimate, configurational averaging over a large number of distributions would be necessary, especially for the smaller sizes, which has been omitted in the present study.

The third important class (right boxes in figure 15) represents the core–shell morphologies. Again, Pt atoms are expected to segregate to the surface, while the Fe atoms occupy predominantly the core sites. For $N = 147$, where Pt covers 80 of the 92 surface sites, this is a very favourable arrangement. For larger clusters, the number of Pt atoms exceeds the number

of surface sites, for $N = 309$ by 3 atoms and by 44 atoms for $N = 561$. Placing these atoms into the subsurface shell, which corresponds to complete segregation, is obviously becoming a much less advantageous structural configuration as demonstrated by the broken red line in figure 15. However, if the subsurface shell is kept Pt depleted and the Pt atoms occupy sites of the third shell instead, the energy is decreased by a sizeable 42 meV/atom. This isomers can also be understood as a shell-wise alternating arrangement of pure Fe and Pt-enriched closed geometric shells with an extreme concentration gradient in the Pt-enriched layers ranging from 0% from the centre to 100% on the surface. In fact, icosahedral configurations with a concentration gradient have been proposed recently to explain high-resolution transmission electron micrographs of larger icosahedral Fe–Pt clusters with a diameter around 6 nm [135]. The stability of onion-ring bimetallic morphologies has been recently discussed for Pd–Pt clusters by means of semi-empirical classical simulation techniques [150–152]. A configuration in which all Pt-containing shells have the same relative composition refers to this limiting case. Corresponding isomers are depicted in figure 15 by triply nested circles and mark the lowest energy isomers throughout the whole investigated size range. This morphology marks an intermediate between core–shell and ordered structures with an incomplete $L1_1$ ordering within each of the 20 twins. The $L1_1$ structure is defined by a layer-wise alternation of [111] planes of the fct lattice occupied by different elements, terminated in our case by the 20 (111) surfaces of the icosahedra. Structures with $L1_1$ ordering are known from the bulk Cu–Pt alloy [153] but not from bulk Fe–Pt or Co–Pt. Here, obviously the low surface energy of the Pt-terminated (111) surfaces overcompensates the energy contributions due to twinning and the strained $L1_1$ arrangement of the core atoms. As a consequence, the energetic advantage over the single crystalline $L1_0$ isomer is decreasing with increasing particle size. A tentative extrapolation according to equation (6) leads to the expectation that the crossover between these two structural motifs will occur around eight closed shells or a diameter around 4 nm, respectively.

Isomers with $N = 147$ atoms or more show a more or less uniform, size independent behaviour for average magnetization per atom [147], which takes values in a corridor of about $\pm 0.1\ \mu_B$ around the average bulk value [154], which is in good agreement with previous DFT studies of unrelaxed Fe–Pt clusters with up to 135 atoms [64]. Exceptions are observed for the core–shell isomers, which show a reduced average moment due to ferrimagnetic alignment of the spins in the Fe-rich core. From DFT calculations it has been predicted [155–158], that the ordered $L1_0$ phase is close to an instability towards an antiferromagnetic (AF) structure described by ferromagnetic (FM) Fe layers alternating along the c-axis. The origin has been traced back to a competition between a Pt-mediated ferromagnetic coupling and a direct antiferromagnetic exchange between the layers [157, 159]. The situation is similar in the α-FeRh alloy, which exhibits a temperature induced AF–FM metamagnetic transition [160]. The hypothetic AF phase of Fe–Pt is characterized by a slightly increased tetragonal distortion with nearly the same atomic volume [158] and accordingly AF isomers have been stabilized in our calculations which are nearly degenerate in energy with their FM counterparts. On the other hand, disorder and magnetocrystalline anisotropy work in favour of the FM phase [148, 155, 156, 161] and entropy may also play a decisive role [159, 162–164].

From the experimental side, it has been argued that an inhomogeneous distribution of the Fe and Pt species may lead to local deviations from the stoichiometric compositions which can decisively influence the magnetic properties of these isomers [120]. A more detailed analysis of the distribution of the magnetic moments with respect to their structural environment is given in figure 16. Here, the site-specific magnetic moments of all Fe and Pt atoms in selected $Fe_{265}Pt_{296}$ particles are plotted versus their distance to the centre of the particle. To provide further information on the structural environment, we use open and filled symbols, alternating with the index n of the geometric shells according to equation (8), to which the respective atoms belong. For all isomers, there is a continuous increase of the iron magnetic moment from the centre of the cluster towards the surface, while the induced Pt moments appear to be nearly constant or even decrease, as for the core–shell morphologies. For the disordered isomers, there are large fluctuations in the Fe and Pt moments owing to the inhomogeneous chemical environment of the Fe atoms. This is greatly reduced for the ordered structures, as there are many equivalent sites, which are consequently characterized by the same magnetic moment and the same distance from the centre. The moment of the central atom is significantly lower in the icosahedral structure, as this position is strongly compressed by the surrounding atoms, which are much closer to the centre than in the cuboctahedral structures. This is a consequence of the fact that the inter-shell atomic distances are about 5% smaller than the intra-shell distances in ideal icosahedra, because all of its neighbours are located in the first shell. Thus for symmetry reasons, there is no possibility for a compensation. The compression is strongest in the case of core–shell isomers which are characterized by a pure iron core with an antiparallel orientation of the first shell. Consequently, the overall diameter of the core–shell icosahedra is about 1–2% smaller than, e.g., for the disordered isomer.

For some of the isomers, the distribution of the positions in figure 16 displays marked deviations from the patterns which are typical for a given morphology. This applies to the fully segregated $Fe_{265}Pt_{296}$ icosahedron and the core–shell cuboctahedron, and is an indication of structural changes. Both isomers are shown as cross-sections in figure 17. While in the first case a shell-wise Mackay transformation of the iron core is observed as described in the last section, the cuboctahedral particle undergoes a (partial) transformation along the Bain path. Common in both cases is that the transforming pure iron core is comparatively small and the presence of chemically mixed shells is not sufficient to prevent the transformations.

4.1.2. Chemical trends on structural stability. One suitable way to search for particles with improved properties with respect to magnetic recording applications, and at the same time to learn more about the physical origin for twinning

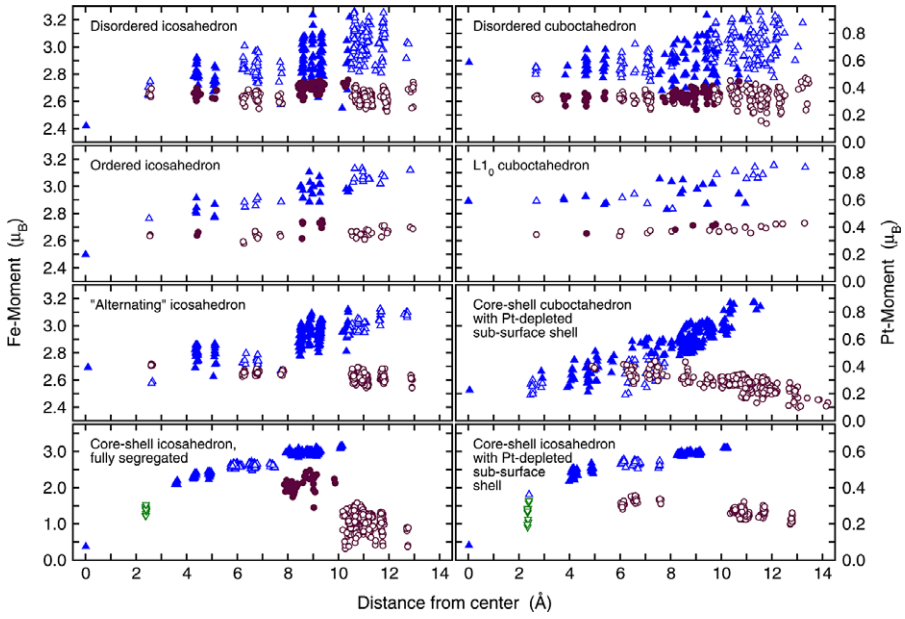

Figure 16. Spatial distributions of the element-specific magnetic spin moments of several $Fe_{265}Pt_{296}$ nanoparticles from figure 15. In addition to these, a core–shell cuboctahedron with Pt-depleted subsurface shell has also been considered. Fe moments are represented by triangles, pointing upwards (blue) for alignment parallel to the total magnetization, downwards (green) for antiferromagnetic alignment. Pt moments are depicted by circles. Moments belonging to geometric shells with even index number n are marked by open symbols, atoms belonging to shells with odd n by filled symbols.

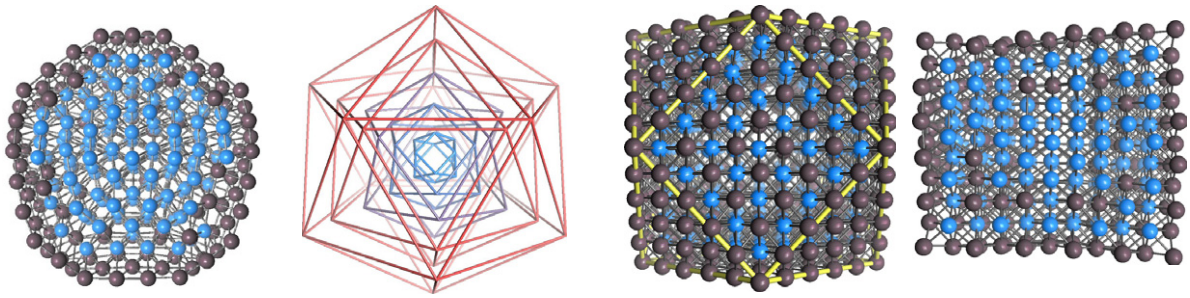

Figure 17. Two examples of structural transformations in chemically inhomogeneous clusters. Left: fully segregated $Fe_{265}Pt_{296}$ icosahedral isomer (cross-section). The edge model obtained in the spirit of figure 7 clearly displays a shell-wise Mackay transformation of the pure iron core. Right: core–shell cuboctahedron with Pt-depleted subsurface shell, full view and cross-section perpendicular to the viewing plane. This isomer is related to the corresponding icosahedral core–shell morphology by a full transformation along the Mackay path and is represented in figure 15 by doubly nested squares. The Fe core transforms along the Bain path, inducing a strong tetragonal distortion of the overall cluster shape.

in FePt particles, is by systematically scanning the periodic table of elements for alternatives. A natural choice is to exchange the 3d element, iron, against the one to its right in the periodic table, cobalt, because bulk $L1_0$ CoPt is known to exhibit a comparably large magnetocrystalline anisotropy and is thus a reasonable choice as recording material as well. Therefore, the investigation on the size dependence of magnetism and structural order has been repeated for Co–Pt in an analogous fashion. Systematic replacements of Pt by other 4d and 5d elements are currently under consideration and will be discussed elsewhere [165]. Figure 18 summarizes the size dependence of the energetic relationship of CoPt clusters for most of the paradigmatic morphologies studied in the preceding section. The energetic order of the morphologies is practically the same as for the Fe–Pt case but appears on a different scale. Again, the $L1_0$ cuboctahedron of the respective size N serves as reference for the energies. In comparison to Fe–Pt, multiply twinned structures have now moved to considerably lower energies. The onion-type $Co_{265}Pt_{296}$ icosahedron, which corresponds to the lowest energy Fe–Pt isomer, lies 90 meV/atom lower in energy. This corresponds to approximately 1000 K (in comparison to ≈330 K in the case of Fe–Pt) and can certainly not be considered in the range of thermal energies. Both segregated morphologies (completely segregated and with Pt-depleted subsurface shell) are even found below. This demonstrates that segregation must be

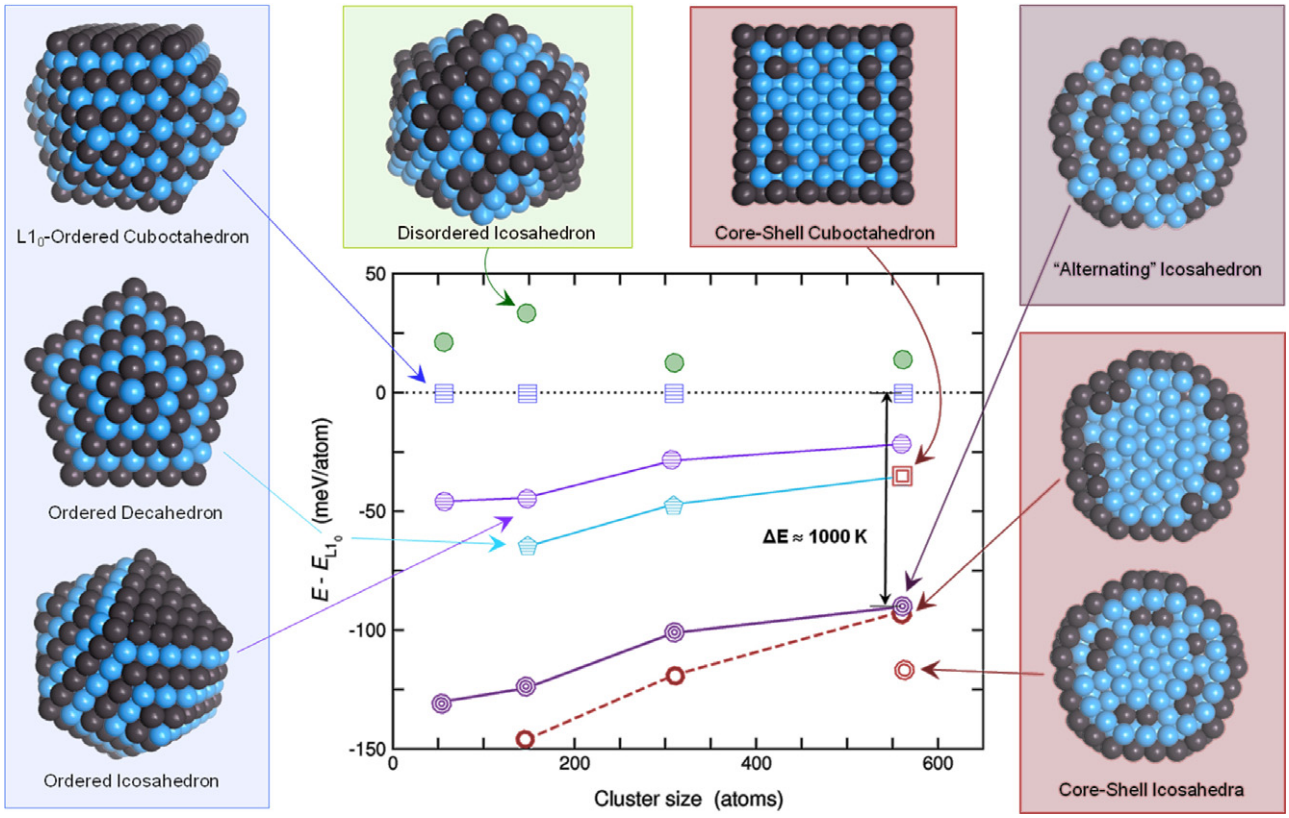

Figure 18. Energies of Co–Pt clusters of various morphologies and sizes. The energy reference is again marked by the $L1_0$ cuboctahedron. Symbols as in figure 15. Data (except for the core–shell cuboctahedron) originally published in [147].

expected to be the dominant mechanism in thermodynamic equilibrium processes. Nevertheless, successful synthesis of single crystalline $L1_0$ Co–Pt particles with diameters of a few nanometres by embedding them into a carbon environment has been reported recently [142, 166]. This stresses the importance of kinetic processes and the interaction with the substrate in this case. The obtained magnetocrystalline anisotropy, however, is still far below the expected values.

A qualitative understanding of the chemical trends on the energetic order of morphologies can be gained from a comparison of the respective element resolved electronic densities of states [147, 149] for Fe–Pt, Co–Pt and Mn–Pt, as shown in figure 19. The DOS of the $L1_0$ ordered $Fe_{265}Pt_{296}$ isomer shares the basic features of bulk $L1_0$-FePt which is already the case for much smaller clusters [64]. Nevertheless, modifications by the surface states are present, which involve 45% of the atoms at this size. For the *alternating* icosahedron and the $L1_0$-ordered cuboctahedron, the Fermi level coincides with minima in the minority spin DOS, arising from the minority spin 3d Fe electrons, reflecting their increased stability with respect to the disordered clusters, where the minimum in the minority spin DOS is completely washed out [149]. This stresses the importance of the 3d electrons of the transition metal element for the stability of the clusters. Indeed, for each morphology, the Pt surface and core contributions remain largely unaltered upon changing the 3d constituent of the clusters.

Additional characteristic features related to the different structures are present in the DOS. In the majority channel of the icosahedron there is a dip around −2.25 eV, surrounded by two maxima, which is only slightly shifted by the replacement of the 3d element. This dip nearly coincides with the hump in the minority channel of the $L1_0$ structures arising from the Pt contributions. Such features could provide a measure to identify or rule out a population of specific morphologies in spectroscopic measurements [167]. As the Pt contribution remains nearly unaffected by changes of the 3d element, a discussion of chemical trends in terms of a simple rigid band picture appears justified. When replacing Fe by Co, the additional d electrons of Co must fill up the states in the minority channel, as the 3d majority states are already occupied. This necessarily shifts the contributions of Co to lower energies. While the electron densities at the Fermi level E_F are nearly the same for both isomers, the density of the $L1_0$ minority 3d states encounters a steep increase above E_F. In consequence, there is a larger shift of the 3d minority states of the icosahedron, which results in a lower contribution to the band energy with respect to the $L1_0$ reference.

This simple relationship between structural stability and the filling of the 3d minority channel suggests that removing 3d minority spin electrons should work in favour of the $L1_0$ structure. This seems indeed to be the case if Fe is completely replaced by Mn. Here, the alternating icosahedron is located approximately 60 meV/atom above the 561-atom $L1_0$ cuboctahedron (as compared to ≈30 meV/atom below for FePt). The ferromagnetic, ordered icosahedron, which is nearly degenerate for $Fe_{265}Pt_{296}$, has become unstable in the Mn–Pt system. During the geometric optimization procedure

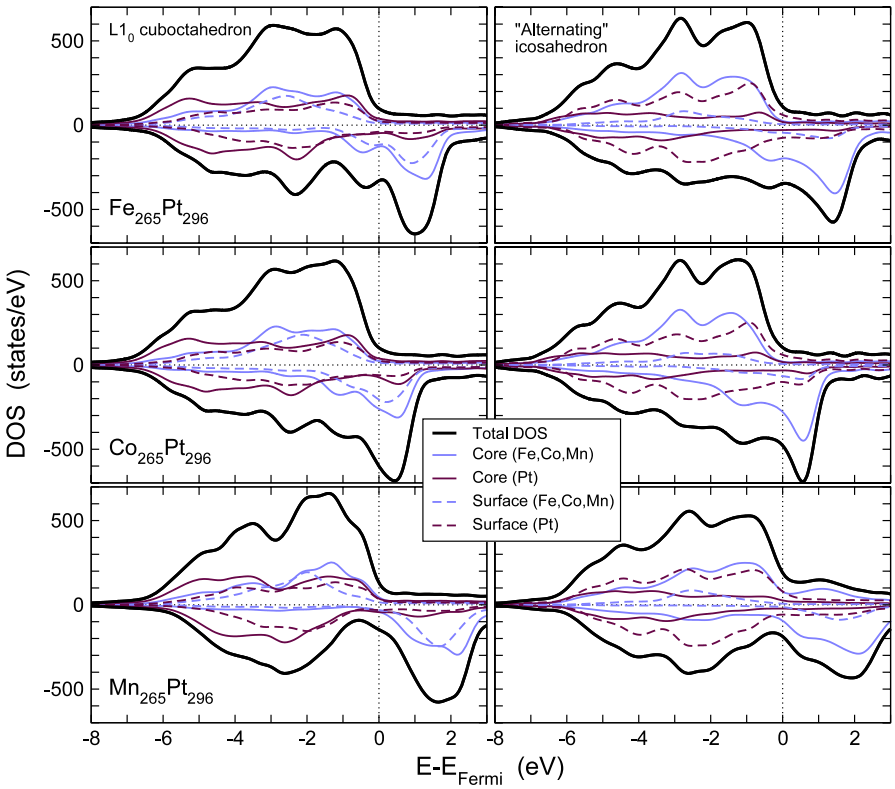

Figure 19. Spin polarized density of states (DOS) of selected $Fe_{265}Pt_{296}$, $Co_{265}Pt_{296}$ and $Mn_{265}Pt_{296}$ morphologies ($L1_0$ ordered cuboctahedron and icosahedron with alternating Fe/Co/Mn and Pt shells) according to figures 15 and 18. The thick full lines denote the total DOS, the thinner full lines the element-specific contributions of the 309 core atoms: bright (blue) lines represent Fe/Co/Mn, dark (brown) lines Pt. Dashed lines describe the contributions of the 252 surface atoms.

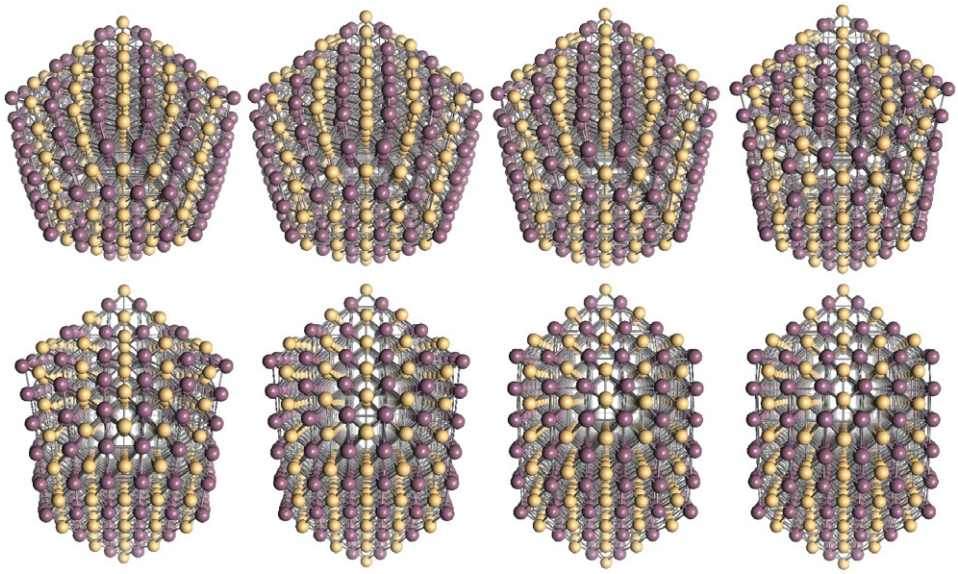

Figure 20. Snapshots of an MnPt cluster transforming from the ordered icosahedral structure (upper left) to the $L1_0$ ordered cuboctahedron (lower right) during the conjugate gradient structure optimization. The snapshots were taken consecutively every 100 optimization steps. Bright (yellow) spheres denote Mn atoms, dark (red) ones Pt atoms.

it transforms downhill to a perfect $L1_0$ cuboctahedron, proving that the Mackay path is a realistic transformation path for magic number transition metal systems (figure 20). Nevertheless, the simple rigid band picture does not hold quite as nicely as for the replacement of Fe by Co. For the alternating icosahedron, e.g., antiferromagnetic alignment of parts of the Mn spins could not be avoided, leading to respective contributions in the majority channel above the Fermi level and in the minority channel below, which alter the overall shape of the total DOS.

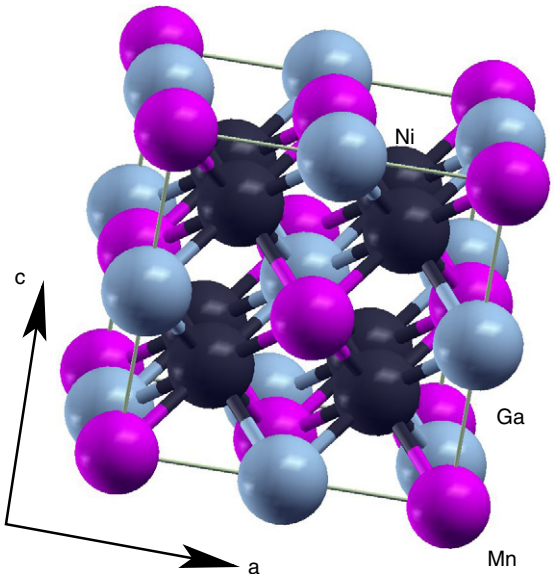

Figure 21. $L2_1$ Heusler structure of austenitic Ni_2MnGa. Black spheres represent Ni, dark (purple) spheres Mn and bright (blue) spheres Ga. Depending on temperature and stoichiometry, tetragonal martensitic phases exist with $c/a \approx 1.2$–1.25 as well as commensurate and incommensurate modulated phases with $c/a = 0.9$–0.94.

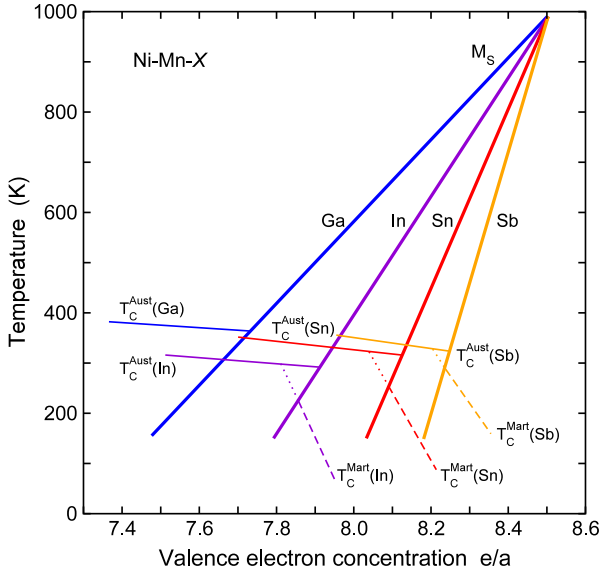

Figure 22. Magnetic and structural phase diagram of the full-Heusler alloys Ni–Mn–X (with X = Ga, In, Sn, Sb) as a function of the composition, given here in terms of the valence electron concentration e/a. The valence electron concentrations of the stoichiometric compounds Ni_2MnX are $e/a = 7.5, 7.5, 7.75, 8.0$ for X = Ga, In, Sn, Sb, respectively. Shown are the martensitic start temperature, M_S, and the Curie temperatures of the austenitic and the martensitic phases, T_C^{Aust} and T_C^{Mart}. Figure adapted from [168].

The drawback in using Mn as stabilizing agent for $L1_0$ particles for magnetic recording purposes is its preference for antiferromagnetic ordering, which is well known for the bulk system and also present in nanoparticles. The lowest energy isomer found so far is an $L1_0$ cuboctahedron with staggered antiferromagnetic arrangement of the spins within the Mn layers. In order not to elicit the latent antiferromagnetic tendencies which are present in pure Fe–Pt as discussed above, only small admixtures of Mn might therefore be admissible to increase the stability of the $L1_0$ phase.

5. Magnetic shape memory alloys—a new class of magnetomechanical actuators

Functional magnetic materials in a more conservative sense of the definition are materials where changes in magnetism—induced, e.g., by an external magnetic field—directly relate to changes in other properties of interest, such as spatial extension, or vice versa. One good example in this respect is magnetic shape memory (MSM) alloys, which transform martensitically below the Curie temperature into the ferromagnetic (FM) state. They represent a new class of actuators, which allow for giant magnetic field induced strains (MFIS) of up to about 10% in Ni_2MnGa [9, 169, 170]. These strains are associated with the super-elastic motion of twin boundaries in the modulated martensitic phases. In prototype Ni_2MnGa, the martensitic phase is stable up to about 274 K, before transforming into the austenitic $L2_1$ phase (cf. figure 21), but the transformation temperature can be shifted above room temperature by changing stoichiometry. In between for near-stoichiometric compositions, a pre-martensitic phase is encountered, which shares the cubic lattice parameters but shows a threefold modulation of

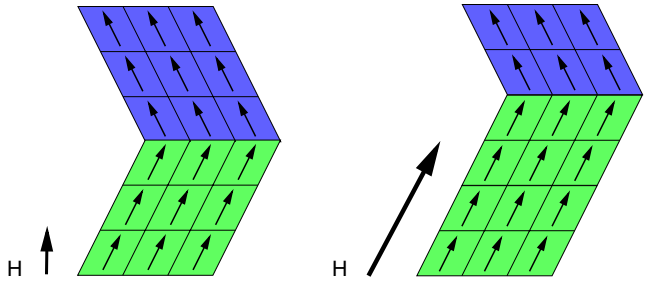

Figure 23. Schematic visualization of the magnetic shape memory effect (magnetic field induced reorientation). Applying a magnetic field favours the martensitic twins with their easy axis parallel to this direction, causing a large magnetic field induced strain (MFIS).

the atomic positions. In the martensitic phases different modulations are observed; frequent are fivefold modulated tetragonal or sevenfold modulated orthorhombic structures. At very low temperatures and off-stoichiometric compositions a non-modulated phase also exists, with a c/a-ratio of around 1.25. The dependence of magnetic and structural phase transition temperatures on the composition is shown schematically in figure 22. Depending on temperature and composition, Ni–Mn–Ga exhibits in addition a variety of martensitic phases, each with different relevance to the MSM effect (see, e.g., [171–173]). Another important aspect, common to most MSM materials, is their comparatively large magnetocrystalline anisotropy in the martensitic phases (see, e.g., [174]). Together with the low activation energy for twin boundary motion, this is considered a key ingredient for the reversible growth of one martensitic variant at the expense of another in MSM alloys, as sketched in figure 23, which leads

to the reported large strains. This MSM mechanism is usually referred to as *magnetic field induced reorientation* (MIR). There is another mechanism called *magnetic field induced martensite* (MIM), which can occur when martensitic and magnetic phase boundaries are coupled (for an introduction, see [175]). Such transitions do not necessarily require large uniaxial magnetocrystalline anisotropies and a high mobility of twin boundaries, but rather a martensitic transition temperature in the desired operation range and a large change in magnetization between both phases. In this case, the introduction of a sufficiently strong magnetic field can shift the martensitic transition temperatures and thus reversibly induce a martensitic transition. This effect was observed in polycrystalline Ni–Mn–In with an MFIS comparable to other polycrystalline MSM alloys [176, 177].

The development of novel sensor and actuator systems based on the MSM effect currently concentrates on two classes of materials: the archetypical Ni-based full-Heusler alloys and Fe–Pd-based alloys [178] close to the bcc–fcc martensitic transformation. Although the Heusler systems are currently the best studied MSM materials, several problems are to be solved before they can be used at a large scale for industrial grade applications. First, the martensitic and magnetic transition temperatures are, although above room temperature in many cases, still too low for many fields of application, e.g. in the automotive sector. Furthermore, the material is very brittle and thus difficult to handle. For large strains, single crystals are needed, which are difficult and expensive to produce. The Fe-based systems have far better mechanical properties; the bio-compatibility of Fe and Pd entitles them for applications within the human body. The Curie temperatures are sufficiently large. However, the required reversible martensitic transition from the austenitic face centred cubic (fcc) to the intermediate martensitic face centred tetragonal (fct) phase, which is relevant for the MSM effect, takes place at even lower temperature than in the Ni–Mn–Ga system [179]. Fe-based MSM systems known so far are based on disordered $Fe_{70}Pd_{30}$ alloys, ordered Fe_3Pt and also Fe–Ni–Co alloys with an addition of a few at.% Ti [180]. However, the considerable MFIS observed in the former two, 3.0% for Fe–Pd and 2.3% For Fe_3Pt, is reported for prohibitively low temperatures of 77 K and 4 K, respectively [181–183]. At higher temperatures, approaching the austenitic phase, the MFIS decreases, as does also the c/a ratio, which determines the upper limit of the achievable strain. Electronic structure calculations [184–186] reveal that a band-Jahn–Teller mechanism is responsible for the transition from the fcc to the fct phase. A similar mechanism is made responsible for the martensitic transition in Heusler-based shape memory alloys [187].

Many essential properties of MSM alloys have been successfully characterized up to now (for a review of previous experimental and theoretical work, see [1, 8–10, 168]). However, one of the central questions, that remains unanswered up to now and is thus a central part of our research, is about the origin of the high mobility of the twin boundaries and how a magnetic field allows us to introduce large magnetic strains in MIR. Other important questions tackle the applicability of the materials, e.g., the shifting of the transition temperatures of the magnetic and structural phase transitions into the desired range or the optimization of the actuator properties in sub-Tesla magnetic fields. Within this review, we will concentrate on two aspects of the Ni–Mn–Ga system, namely the relationship between magnetism and phase stability and the influence of changes in stoichiometry on the mobility of twin boundaries.

5.1. Magnetism and phase stability in MSM Heusler alloys

The complex relationship between the austenitic and the various martensitic phases which are present in MSM Heusler alloys has been subjected to numerous theoretical and experimental studies. Concerning the former, there has been strong emphasis on first-principles DFT calculations with respect to structure and magnetism [188–197], electronic properties and Fermi surface nesting [198–204], and thermal properties and lattice dynamics [199, 200, 204–210]. Especially the latter aspect goes hand in hand with large endeavours in experiment related to the temperature dependent anomalies in the austenitic phonon dispersions when approaching the (pre-)martensitic transition temperature. This shows up as a temperature dependent (incomplete) softening of the TA_2 branch in the [110] direction at a fraction of $\xi \approx 1/3$ of the way between the Γ- and the X-point of the Brillouin zone [211–216]. The instability of the TA_2 branch has been related to nesting features of the Fermi surface in the austenitic phase in the literature (see, e.g., [199, 200, 203, 217]). The phonon anomalies can be reproduced by DFT calculations [192, 200], but the softening is complete here, i.e it leads to imaginary frequencies. On the other hand, the calculations refer to $T = 0$, where the cubic $L2_1$ structure of the austenitic phase should in fact be unstable. The contribution due to electron–phonon coupling to the dynamical matrix $\underline{\underline{D}}(\underline{q})$ defined in equation (4) is given by the following expression [218, 219]:

$$D^{\alpha\beta}_{\mathrm{el-ph}}(\underline{q}) = \sum_{\underline{k},n,m} \frac{f(\varepsilon_{\underline{k},m})(1 - f(\varepsilon_{\underline{k}+\underline{q},n}))}{\varepsilon_{\underline{k}+\underline{q},n} - \varepsilon_{\underline{k},m}} \times g^{\alpha *}_{\underline{k},m,\underline{k}+\underline{q},n}\, g^{\beta}_{\underline{k}+\underline{q},n,\underline{k},m}, \tag{14}$$

where f is the Fermi distribution function and $\varepsilon_{\underline{k},m}$ are the energies of band m at the reciprocal vector $\underline{k}$. The g denote the matrix elements describing the strength of the electron–phonon-coupling. As these are difficult to calculate and in many cases only a little variation is expected, they are often set to unity. The resulting expression is then termed as generalized susceptibility $\chi(\underline{q})$.

One central aspect of our work on Heusler alloys is to understand the relation between magnetism and the complex sequence of phases as a function of temperature. Such a relation has been first proposed by Lee *et al* [199]. Later on, the energy landscape and the phonon spectra were evaluated for different magnetizations by using the fixed spin moment (FSM) method [220]. These calculations highlight the importance of magnetic order as a stabilizing feature of the austenitic phase [209]. Consequently, we also examined the system at smaller values than the equilibrium moment of Ni_2MnGa [194]. This can be justified by a closer look

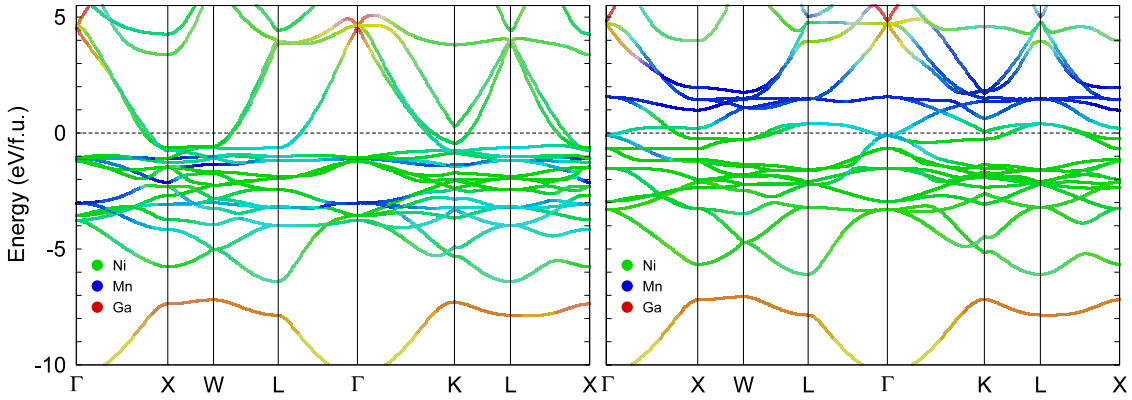

Figure 24. Element resolved band structure of Ni_2MnGa for the majority (left) and the minority spin channel (right). The colour coding refers to the contribution of the specified elements. Mixed contributions are marked by intermediate colours.

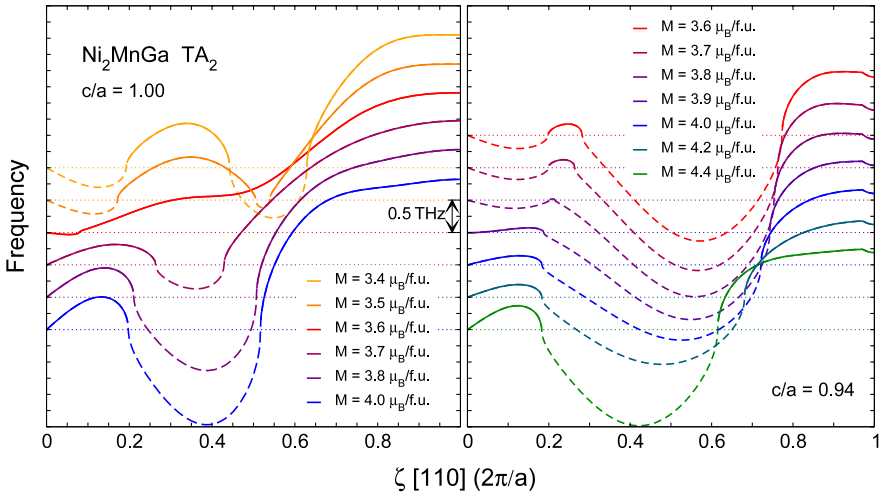

Figure 25. TA_2 branch of the phonon dispersion curves of cubic $L2_1$ (left) and unmodulated tetragonal Ni_2MnGa with $c/a = 0.94$ (right) calculated along the [110] direction for different fixed magnetic moments. To improve visibility, the individual branches are shifted in energy; unstable parts (imaginary frequencies) are denoted by broken lines. For the $L2_1$ case, the branches for 3.6 μ_B/f.u. are nearly stable. The equilibrium moment is 4.06 μ_B per formula unit.

at the spin and element resolved band structure of Ni_2MnGa (figure 24). Gallium states are mainly present several eV below and above the Fermi level and are important to stabilize the Heusler-type structure. Manganese contributions are predominantly found below the Fermi level (in the majority channel) or above (in the minority channel). Except for a small portion around the Γ-point, the Fermi surface is dominated by Ni states in both minority and majority spin channels, so that subtle changes of the exchange splitting can have decisive effects on the Fermi surface. This can be easily modelled in a Stoner-like approach, focusing on the description on the magnetism of the Ni atoms. The Ni atoms do not develop a stable magnetic moment on their own, as the coordination of the Ni atoms in austenitic $L2_1$ Ni_2MnGa is rather body centred cubic than face centred cubic. The observed Ni moments are induced by the surrounding Mn atoms and these exhibit a stable, rather localized moment, which has been shown in detail by non-collinear spin-spiral calculations [191]. The Mn states, on the other hand, which are represented less well by the present approach, are not expected to take part in the instabilities leading to the reconstruction of the Fermi surface.

For the resulting phonon dispersions, we found in the austenitic phase a narrow region around 3.6 μ_B/f.u., in which the instability at finite $\xi \approx 0.4$ disappears (figure 25). This is only 10% below and thus in the realistic vicinity of the ground state magnetization of 4.06 μ_B/f.u. and corresponds to a region of the binding surface where the $L2_1$ austenite and the non-modulated $L1_0$ martensite are close in energy, separated only by a tiny energy wall [194]. In the unmodulated tetragonal structures with $c/a = 0.94$, the instability at finite ξ is present for all magnetizations, but varies its position. This is in accordance with the observation that the pseudo-tetragonal martensite with $c/a = 0.94$ is only stable because of magnetism and modulations in the atomic positions [204, 206, 208]—in contrast to the martensitic $L1_0$ structure with $c/a \approx 1.25$, which is found to be stable at very low temperatures or off-stoichiometric compositions. All of these results demonstrate the extremely close interrelation of electronic structure, magnetism and phase stability in the MSM Heusler systems. This view found recent support from *ab initio* free energy calculations [210] obtained within the quasiharmonic approximation given in equation (5).

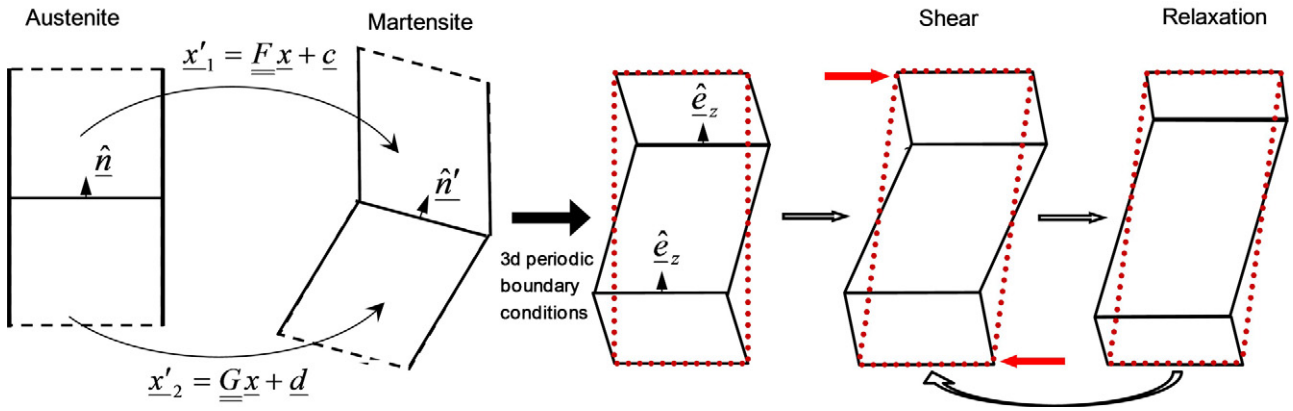

Figure 26. Schematic sketch visualizing the construction of an atomistic twin boundary model for the martensitic phase, which is compatible with three-dimensional periodic boundary conditions, and the simulation of twin boundary movement by repeated shearing of the cell and relaxation of the atomic positions as performed in our calculations.

Comparison of the free energies of austenite, the threefold modulated pre-martensite and non-modulated $L1_0$ martensite calculated for the ground state magnetic moment of the respective phases yields a reasonable transition temperature between martensite and pre-martensite, while the austenite never becomes stable, which is in blatant disagreement with experiment. In turn, considering finite temperature magnetic excitations according to the experimental magnetization curves within the FSM stabilizes the austenite at finite temperatures and thus re-establishes the experimental sequence of phases. However, to finally conclude on the precise relationship between Fermi surface nesting, magnetism and structural stability requires a detailed statistical analysis of the generalized susceptibility with respect to phonon vectors $\underline{q}$ in combination with a first-principles evaluation of the respective electron–phonon coupling matrix elements.

5.2. *Twin boundary mobility in magnetic shape memory alloys*

The natural approach to look at finite temperature properties, which is also well suited to provide insight into the origin of the high mobility of twin boundaries on the atomistic level, would be, again, classical molecular dynamics simulations. These allow us to deal with a sufficiently large number of atoms, but depend on the availability of reliable empirical model potentials. For the case of MSM alloys, up to now, in either the Heusler-type or the Fe-based systems, suitable model potentials still do not exist and their development is a very delicate task, since the martensitic instability is closely related to the details of the electronic structure as shown above. Therefore, it remains necessary to perform *ab initio* molecular dynamics simulations to look at the materials properties on the atomistic scale. Within this context, in a first step, the mathematical framework for simulating shear induced twin boundary mobility was set up making use of the continuum theory of martensitic transformations [221] and performing first *ab initio* simulations of comparatively small systems (256 atoms) [222] for the non-MSM relevant $L1_0$ phase as a test case. These calculations have meanwhile been extended to larger and non-stoichiometric systems.

As the material undergoes a martensitic transformation from a high-symmetry parent phase at higher temperatures to a low-symmetry low-temperature phase, so-called twinning will occur. This is due to the different spatial possibilities in which the low-symmetry phase can nucleate from the parent phase at the spatially separated seeds for the martensitic transformation. Following the continuum theory of martensitic transformations [221, 223, 224], the diffusionless, displacive motion of an atom from position $\underline{x}$ to $\underline{x}'$ is represented by a homogeneous transformation, defined by a matrix $\underline{\underline{F}}$ and a vector $\underline{c}$:

$$\underline{x}' = \underline{\underline{F}}\,\underline{x} + \underline{c}, \tag{15}$$

and, eventually, by an additional shuffle. In general, different representations for such homogeneous transformations are encountered, typically connected by symmetry operations, e.g. a rotation $\underline{\underline{Q}}$, which is part of the point group of the parent phase but not of martensite, giving rise to martensitic twinning. The condition of kinematic compatibility assures that a line crossing the twin boundary between two regions represented by $\underline{\underline{F}}$ and $\underline{\underline{G}}$ remains unbroken:

$$\underline{\underline{Q}}\,\underline{\underline{F}} - \underline{\underline{G}} = \underline{a} \otimes \hat{\underline{n}}. \tag{16}$$

The vector $\underline{a}$ and the normal vector of the twin boundary plane $\hat{\underline{n}}$ are given by the following equations:

$$\underline{a} = |\underline{n}|\left(\sqrt{\frac{\lambda_3\,(1-\lambda_1)}{\lambda_3-\lambda_1}}\,\hat{\underline{e}}_1 \pm \sqrt{\frac{\lambda_1\,(1-\lambda_3)}{\lambda_3-\lambda_1}}\,\hat{\underline{e}}_3\right), \tag{17}$$

$$\hat{\underline{n}} = \frac{1}{|\underline{n}|}\,\frac{\sqrt{\lambda_3}-\sqrt{\lambda_1}}{\sqrt{\lambda_3-\lambda_1}} \times (-\sqrt{1-\lambda_1}\,\underline{\underline{G}}^{\mathrm{T}}\,\hat{\underline{e}}_1 \pm \sqrt{\lambda_3-1}\,\underline{\underline{G}}^{\mathrm{T}}\,\hat{\underline{e}}_3), \tag{18}$$

if an ordered set of eigenvalues $\lambda_1 \leqslant \lambda_2 = 1 \leqslant \lambda_3$ of $\underline{\underline{C}} = \underline{\underline{G}}^{-\mathrm{T}}\,\underline{\underline{F}}^{\mathrm{T}}\,\underline{\underline{F}}\,\underline{\underline{G}}^{-1}$ exists [223]; $\hat{\underline{e}}_1$ and $\hat{\underline{e}}_3$ refer to the corresponding eigenvectors. This information can be used to construct a model of a perfect martensitic twin boundary suitable for atomistic simulations as depicted in figure 26 (left). Compatibility with the periodic boundary conditions can be achieved by rotating the system so that the twinning

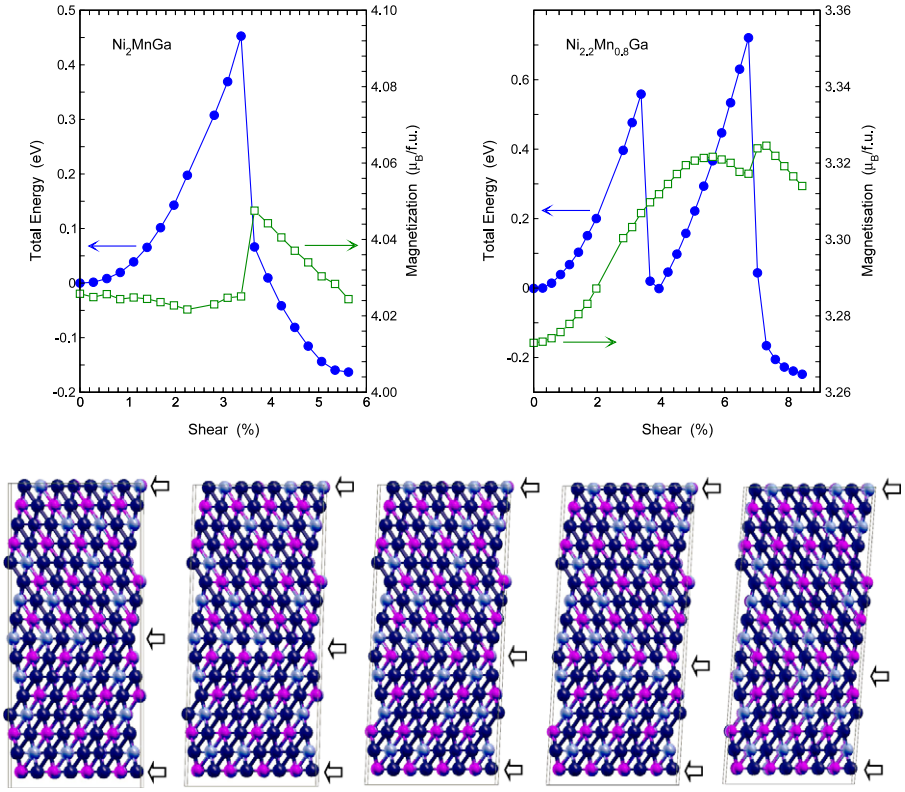

Figure 27. Total energy and magnetic moment are given as a function of the shear of the simulation cell for each completed quasistatic relaxation step for stoichiometric Ni_2MnGa (left) and off-stoichiometric $Ni_{2.2}Mn_{0.8}Ga$ (right). Bottom: selected configurations (energy minima and transition states) of the 512-atom $Ni_{2.2}Mn_{0.8}Ga$ supercell resulting from the geometric optimization processes after applying shear on the simulation box (in the horizontal direction). The arrows denote the positions of the twin boundaries. Black spheres represent Ni, dark (purple) spheres Mn and bright (blue) spheres Ga.

plane given by $\hat{\underline{n}}$ is parallel to one of boundary planes of the simulation cell. The periodic boundary conditions also imply that there are at least two twin boundaries in the simulation cell. For the transformation to the $L1_0$ structure, the transformation matrix can be chosen in analogy to the Bain path as a (volume conserving) diagonal matrix with one of the diagonal elements different from the other two. For the transformation to the pseudo-tetragonal structure with $c/a < 1$, we follow the experimental findings from neutron diffraction data that two consecutive shears on (110) planes in the $[\bar{1}10]$ directions are involved [225]. As the direct *ab initio* simulation of twin boundary motion induced by a directional change of magnetic field including spin–orbit interactions exceeds the current possibilities, we induce twin boundary motion by applying shear on the simulation cell. The induced stress is resolved in a subsequent relaxation step, as sketched in figure 26 (right), eventually leading to the introduction of defects or a shift of the twinning plane. Then, in a number of consecutive shear and relaxation steps, a quasistatic picture of twin boundary motion can be constructed.

Figure 27 shows the result of such a procedure applied to stoichiometric Ni_2MnGa and off-stoichiometric $Ni_{2.2}Mn_{0.8}Ga$. Here, a supercell containing 512 atoms and two martensitic variants was used, the latter with a width of four unit cells each. The magnetization shows—unlike in our previous simulations with 256 atoms [222]—only a small variation before and after the shifting process, indicating that finite size effects are considerably decreased and cells of 512 atoms may be sufficient to study the shear induced coherent motion process of the twin boundary. The activation energy in figure 27 is of the same magnitude as in the smaller case, being one order larger than the MAE per atom multiplied by the system size [174, 222]. Disorder apparently does not change the energy scale. However, in the stoichiometric case, both twin boundaries move at the same time, whereas in the off-stoichiometric case, the same twin boundary (in the centre) moves in two consecutive steps, while the other (at the cell boundary) remains immobile. The observed energy scale is in accordance with experimental observations and energetic considerations by Kakeshita *et al* [183, 226, 227] of $Ni_{2.14}Mn_{0.92}Ga_{0.94}$ in the $L1_0$ phase with $c/a \approx 1.20$ and corroborates our previous finding, that despite its considerably larger magnetocrystalline anisotropy for the $L1_0$ phase with the large c/a ratio a magnetic field induced (coherent) rearrangement of twins is not a realistic process for this phase. It has to be noted at this point that the current understanding is that interface defects like disconnections play a decisive role for the motion of realistic interfaces between phases and twins (see [228, 229] for recent reviews). Corresponding simulations require very large cells, containing more than 10 000 atoms, and are currently only feasible on the basis of classical molecular dynamics simulations. As discussed above, it is

unclear whether accurate empirical potentials can be developed soon. Thus, for now, only first-principles calculations can bring forward the understanding of the atomistic processes at the interface and might serve as helpful benchmarks in future.

While these results are encouraging in the sense that *ab initio* simulations of twin boundary mobility are possible, they also show that it is essential to explicitly consider the modulated phases, as attempts to approximate these by an unmodulated pseudo-tetragonal structure lead to a complete dissolution of the interfaces. This is related to the unstable phonon dispersions shown in figure 25 and demonstrates that the relevant processes are taking place on a fairly small energy scale. The consideration of the rather large modulated unit cells and the required increase in numerical accuracy will boost the numerical demands, showing, once again, the importance of state-of-the-art high-performance computing for practical materials science applications.

6. Conclusions

Performing full structural optimizations of systems containing up to 923 spin-polarized transition metal atoms, we demonstrated in three examples how nanometre-scale first-principles investigations on contemporary state-of-the-art supercomputers contribute to the understanding of key properties of functional magnetic materials of technological interest.

- Iron clusters from around $N \approx 100$ atoms upwards have a bcc structure in the ground state. Icosahedra and cuboctahedra are unstable against a partial transformation along the Mackay path. For $N = 55$, a shell-wise Mackay-transformed structure is a good candidate for the ground state and lies within the range of thermal energies for larger sizes. While retaining an icosahedral outer shape, this structure is characterized by a fcc-like coordination of the cluster core and bcc-like coordination of the subsurface atoms; the corresponding pair distribution function exhibits typical features of amorphous systems. Due to the ferrimagnetic alignment of the spins in the core, the magnetic moment of this morphology is for $N = 561$ in much better agreement with the experimental data than the bcc isomers.
- For magic number Fe–Pt and Co–Pt nanoclusters, which are of technological interest for ultra-high density magnetic recording applications in their single crystalline $L1_0$ phase, multiply twinned morphologies are energetically favoured up to diameters of at least 3 nm. The lowest energy morphology found for Fe–Pt is an onion-type structure with alternating Fe- and Pt-rich shells and a Pt-covered surface. For Co–Pt, segregated icosahedral morphologies are even more favoured, exceeding the range of thermal energies with respect to the $L1_0$ reference structure. A comparison of the electronic densities of states suggests that the tendency to form multiply twinned morphologies can be controlled by the filling of the 3d minority spin channel. Consequently, multiply twinned morphologies are found to be suppressed in the case of Mn–Pt nanoclusters. Here, a staggered antiferromagnetic $L1_0$ structure is found to be lowest in energy.
- To address the mobility of twin interfaces in Ni_2MnGa shape memory alloy in its various phases, we proposed a simulation scheme, which allows us to get microscopic insight into a stress induced martensitic reorientation process in Ni_2MnGa by means of *ab initio* molecular statics calculations. Relating the results of the quasistatic simulations of shear induced twin boundary motion in the $L1_0$ phase with $c/a \approx 1.25$ to previous calculations of the magnetocrystalline anisotropy energy, we see that the energy scales encountered in the coherent reorientation processes of twins and magnetization are not of the same order of magnitude. So far, the simulations are restricted to—still—comparatively small system sizes and defect-free interfaces. The experimentally observed modulation in the pseudo-tetragonal and orthorhombic phases with $c/a < 1$, which are the relevant ones for the MSM effect, should also be taken into account. All of these amendments are connected with increased numerical demands and still left open for future investigations.

Despite all the benefits which can be expected from the applications point of view, it should be acknowledged that the developers of the DFT packages on the other hand are confronted with the Sisyphean challenge to constantly adapt their codes in order to keep their parallel performance in pace with an exponential development of computing resources. However, regarding the perspectives for the field of materials science, this might be worth the effort. There is plenty of room at the TOP500.

Acknowledgments

The vast majority of the calculations has been performed on the IBM Blue Gene/L and Blue Gene/P supercomputers of the John von Neumann Institute for Computing (NIC) in Jülich. Without the access to these resources, the work presented above certainly would not have been possible. We thank the staff of the Jülich Supercomputing Centre (JSC) and IBM for their continuous support, especially P Vezolle (IBM) and I Gutheil (JSC) for their substantial help in making the VASP code run efficiently on the Blue Gene systems. This work also depends on many stimulating discussions and helpful comments. In this respect we would like to gratefully acknowledge the contributions of G Rollmann, A Hucht, R Meyer, J R Chelikowsky and M L Tiago (iron nanoparticles), M Farle, O Dmitrieva, D Sudfeld, N Friedenberger, C Antoniak, M Spasova, K Albe and U Wiedwald (binary particles for ultra-high density magnetic recording) and A T Zayak, W A Adeagbo, U K Rößler, I Opahle, M Richter, R C Pond, S Fähler, M Acet and E F Wassermann (magnetic shape memory Heusler alloys). The illustrations in figures 14, 21 and 27 (bottom) have been created using the XCrySDen visualization software [230]. The authors would also like to thank the Psi-k network [231] for the kind invitation to present our work to the European electronic structure community as part of their bi-monthly

newsletter. Financial support was granted by the Deutsche Forschungsgemeinschaft through the Priority Programme SPP 1239, *Change of microstructure and shape of solid materials by external magnetic fields*, and SFB 445, *Nanoparticles from the gas phase: formation, structure, properties*.

References

[1] Planes A, Mañosa L and Saxena A (ed) 2005 *Magnetism and Structure in Functional Materials* (*Springer Series in Materials Science* vol 79) (Berlin: Springer)
[2] Pankhurst Q A, Conolly J, Jones S K and Dobson J 2003 Application of magnetic nanoparticles in biomedicine *J. Phys. D: Appl. Phys.* **36** R167
[3] Tartaj P, del Puerto Morales M, Veintemillas-Verdaguer S, Gonzáles-Carreño T and Serna C J 2003 The preparation of magnetic nanoparticles for application in biomedicine *J. Phys. D: Appl. Phys.* **36** R182
[4] Šafařík I and Šafaříková M 2002 Magnetic nanoparticles and biosciences *Monatsh. Chem.* **737** 133
[5] Sun S, Murray C B, Weller D, Folks L and Moser A 2000 Monodisperse FePt nanoparticles and ferromagnetic FePt nanocrystal superlattices *Science* **287** 1989
[6] Sun S 2006 Recent advances in chemical synthesis, self-assembly, and applications of FePt nanoparticles *Adv. Mater.* **18** 393
[7] Weller D and Moser A 1999 Thermal effect limits in ultrahigh-density magnetic recording *IEEE Trans. Magn.* **35** 4423
[8] Vasil'ev A N, Buchel'nikov V D, Takagi T, Khovailo V V and Estrin E I 2003 Shape memory ferromagnets *Phys.—Usp.* **46** 559
[9] Söderberg O, Ge Y, Szinov A, Hannula S P and Lindroos V V 2005 Recent breakthrough development of the shape memory effect in Ni–Mn–Ga alloys *Smart Mater. Struct.* **14** 223
[10] Entel P, Buchelnikov V D, Khovailo V V, Zayak A T, Adeagbo W A, Gruner M E, Herper H C and Wassermann E F 2006 Modelling the phase diagram of magnetic shape memory heusler alloys *J. Phys. D: Appl. Phys.* **39** 865
[11] Pastor G M, Dorantes-Dávila J and Bennemann K H 1989 Size and structural dependence of the magnetic properties of small 3d-transition-metal clusters *Phys. Rev.* B **40** 7642
[12] Andriotis A N and Menon M 1998 Tight-binding molecular-dynamics study of ferromagnetic clusters *Phys. Rev.* B **57** 10069
[13] Barreteau C, Desjonquieres M and Spanjaard D 2000 Theoretical study of the icosahedral to cuboctahedral structural transition in Rh and Pd clusters *Eur. Phys. J.* D **11** 395
[14] Guirado-López R A, Dorantes-Dávila J and Pastor G M 2003 Orbital magnetism in transition-metal clusters: From Hund's rule to bulk quenching *Phys. Rev. Lett.* **90** 226402
[15] Xie Y and Blackman J A 2004 Universal tight-binding model for transition metals: from bulk to cluster *J. Phys.: Condens. Matter* **16** 8589
[16] Köhler C, Seifert G and Frauenheim T 2006 Magnetism and the potential energy hypersurfaces of Fe_{53} to Fe_{57} *Comput. Mater. Sci.* **35** 297
[17] Dudarev S L and Derlet P M 2005 A 'magnetic' interatomic potential for molecular dynamics simulations *J. Phys.: Condens. Matter* **17** 7097
[18] Ma P W, Woo C H and Dudarev S L 2008 Large-scale simulation of the spin–lattice dynamics in ferromagnetic iron *Phys. Rev.* B **78** 024434
[19] Goedecker S 1999 Linear scaling electronic structure methods *Rev. Mod. Phys.* **71** 1085
[20] Soler J M, Artacho E, Gale J D, Garciá A, Junquera J, Ordejón P and Sánchez-Portal D 2002 The siesta method for *ab initio* order-n materials simulation *J. Phys.: Condens. Matter* **14** 2745
[21] Bowler D R, Choudhury R, Gillan M J and Miyazaki T 2006 Recent progress with large-scale *ab initio* calculations: the CONQUEST code *Phys. Status Solidi* b **243** 989
[22] Ozaki T 2006 $\mathcal{O}(N)$ Krylov-subspace method for large-scale *ab initio* electronic structure calculations *Phys. Rev.* B **74** 245101
[23] Skylaris C K, Haynes P D, Mostofi A A and Payne M C 2008 Recent progress in linear-scaling density functional calculations with plane waves and pseudopotentials: the ONETEP code. *J. Phys.: Condens. Matter* **20** 064209
[24] Zeller R 2008 Towards a linear-scaling algorithm for electronic structure calculations with the tight-binding Korringa–Kohn–Rostoker Green function method *J. Phys.: Condens. Matter* **20** 294215
[25] Gruner M E, Rollmann G and Entel P 2008 Large-scale first-principles calculations of magnetic nanoparticles *Proc. NIC Symposion 2008 (Jülich)* (*NIC Series* vol 39) ed G Münster, D Wolf and M Kremer p 161
[26] www.top500.org
[27] Tomanek D 2005 Carbon-based nanotechnology on a supercomputer *J. Phys.: Condens. Matter* **17** R413
[28] Viñes F, Illas F and Neyman K M 2007 On the mechanism of formation of metal nanowires by self-assembly *Angew. Chem. Int. Edn* **46** 7094
[29] Akola J and Jones R O 2007 Structural phase transitions on the nanoscale: the crucial pattern in the phase-change materials $Ge_2Sb_2Te_5$ and GeTe *Phys. Rev.* B **76** 235201
[30] Akola J and Jones R O 2008 Binary alloys of Ge and Te: order, voids, and the eutectic composition *Phys. Rev. Lett.* **100** 205502
[31] Gygi F *et al* 2006 Large-scale electronic strucutre calculation of high-Z metals on the Blue Gene/L platform *Proc. ACM/IEEE Conf. on Supercomputing (Tampa, FL)*
[32] Gygi F 2008 Architecture of Qbox: a scalable first-principles molecular dynamics code *IBM J. Res. Dev.* **52** 137
[33] Laskowski R, Blaha P, Gallauner T and Schwarz K 2007 Single-layer model of the hexagonal boron nitride nanomesh on the Rh(111) surface *Phys. Rev. Lett.* **98** 106802
[34] Laskowski R and Blaha P 2008 Unraveling the structure of the h-BN/Rh(111) nanomesh with *ab initio* calculations *J. Phys.: Condens. Matter* **20** 064207
[35] Hohenberg P and Kohn W 1964 Inhomogeneous electron gas *Phys. Rev.* **136** B864
[36] Kohn W and Sham L J 1965 Self-consistent equations including exchange and correlation effects *Phys. Rev.* **140** A1133
[37] Souvatzis P, Eriksson O, Katsnelson M I and Rudin S P 2008 Entropy driven stabilization of energetically unstablecrystal structures explained from first principles theory *Phys. Rev. Lett.* **100** 095901
[38] Kresse G and Furthmüller J 1996 Efficient iterative schemes for *ab initio* total-energy calculations using a plane-wave basis set *Phys. Rev.* B **54** 11169
[39] Kresse G and Joubert D 1999 From ultrasoft pseudopotentials to the projector augmented-wave method *Phys. Rev.* B **59** 1758
[40] Hafner J 2008 *Ab initio* simulations of materials using VASP: density-functional theory and beyond *J. Comput. Chem.* **29** 2044
[41] Perdew J P 1991 *Electronic Structure of Solids '91* ed P Ziesche and H Eschrig (Berlin: Akademie)
[42] Perdew J P, Burke K and Wang Y 1996 Generalized gradient approximation for the exchange–correlation hole of a many-electron system *Phys. Rev.* B **54** 16533

[43] Vosko S H, Wilk L and Nusair M 1980 Accurate spin-dependent electron liquid correlation energies for local spin density calculations: a critical analysis *Can. J. Phys.* **58** 1200

[44] Parlinski K, Li Z Q and Kawazoe Y 1997 First-principles determination of the soft mode in cubic ZrO_2 *Phys. Rev. Lett.* **78** 4063

[45] Perdew J P, Burke K and Ernzerhoff M 1996 Generalized gradient approximation made simple *Phys. Rev. Lett.* **77** 3865

[46] Gara A *et al* 2005 Overview of the Blue Gene/L system architecture *IBM J. Res. Dev.* **49** 195

[47] Alonso J A 2000 Electronic and atomic structure, and magnetism of transition metal clusters *Chem. Rev.* **100** 637

[48] Baletto F and Ferrando R 2005 Structural properties of nanoclusters: energetic, thermodynamic, and kinetic effects *Rev. Mod. Phys.* **77** 371

[49] Bansmann J *et al* 2005 Magnetic and structural properties of isolated and assembled clusters *Surf. Sci. Rep.* **56** 189

[50] Binns C *et al* 2005 The behaviour of nanostructured magnetic materials produced by depositing gas-phase nanoparticles *J. Phys. D: Appl. Phys.* **38** R357

[51] Billas I M L, Becker J A, Châtelain A and de Heer W A 1993 Magnetic moments of iron clusters with 25 to 700 atoms and their dependence on temperature *Phys. Rev. Lett.* **71** 4067

[52] Billas I M L, Châtelain A and de Heer W A 1994 Magnetism from the atom to the bulk in iron, cobalt, and nickel clusters *Science* **265** 1682

[53] Billas I M L, Châtelain A and de Heer W A 1997 Magnetism of Fe, Co and Ni in molecular beams *J. Magn. Magn. Mater.* **168** 64

[54] van de Waal B W 1988 Stability of face-centered cubic and icosahedral Lennard-Jones clusters *J. Chem. Phys.* **90** 3407–8

[55] Raoult B, Farges J, de Feraudy M F and Torchet G 1989 Comparison between icosahedral, decahedral and crystalline Lennard-Jones models containing 500 to 6000 atoms *Phil. Mag.* B **60** 881–906

[56] Doye J P K and Calvo F 2001 Entropic effects on the size dependence of cluster structure *Phys. Rev. Lett.* **86** 3570

[57] Shao X, Xiang Y and Cai W 2005 Structural transition from icosahedra to decahedra of large Lennard-Jones clusters *J. Phys. Chem.* A **109** 5193–7

[58] Cleveland C L and Landmann U 1991 The energetics and structure of nickel clusters: size dependence *J. Chem. Phys.* **94** 7376

[59] Schebarchov D and Hendy S C 2006 Superheating and solid–liquid phase coexistence in nanoparticles with nonmelting surfaces *Phys. Rev. Lett.* **96** 256101

[60] Duan H M and Zheng Q Q 2001 Symmetry and magnetic properties of transition metal clusters *Phys. Lett.* A **280** 333

[61] Postnikov A V, Entel P and Soler J M 2003 Density functional simulation of small Fe nanoparticles *Eur. Phys. J.* D **25** 261

[62] Šipr O, Košuth M and Ebert H 2004 Magnetic structure of iron clusters and iron crystal surfaces *Surf. Sci.* **566–568** 268

[63] Šipr O, Košuth M and Ebert H 2004 Magnetic structure of free iron clusters compared to iron crystal surfaces *Phys. Rev.* B **70** 174423

[64] Ebert H, Bornemann S, Minár J, Dederichs P H, Zeller R and Cabria I 2006 Magnetic properties of Co- and FePt-clusters *Comput. Mater. Sci.* **35** 279

[65] Futschek T, Marsman M and Hafner J 2005 Structural and magnetic isomers of small Pd and Rh clusters: an *ab initio* density functional study *J. Phys.: Condens. Matter* **17** 5927

[66] Futschek T, Hafner J and Marsman M 2006 Stable structural and magnetic isomers of small transition-metal clusters from the Ni group: an *ab initio* density-functional study *J. Phys.: Condens. Matter* **18** 9703

[67] Kumar V and Kawazoe Y 2002 Icosahedral growth, magnetic behavior, and adsorbate-induced metal–nonmetal transition in palladium clusters *Phys. Rev.* B **66** 144413

[68] Kumar V and Kawazoe Y 2001 Evolution of electronic states and abnormal multishell relaxations in strontium clusters *Phys. Rev.* B **63** 075410

[69] Nava P, Sierka M and Ahlrichs R 2003 Density functional study of palladium clusters *Phys. Chem. Chem. Phys.* **5** 3372

[70] Tiago M L, Zhou Y, Alemany M M G, Saad Y and Chelikowsky J R 2006 Evolution of magnetism in iron from the atom to the bulk *Phys. Rev. Lett.* **97** 147201

[71] Guevara J, Parisi F, Llois A M and Weissmann M 1997 Electronic properties of transition-metal clusters: consideration of the spillover in a bulk parametrization *Phys. Rev.* B **55** 13283

[72] Franco J A, Vega A and Aguilera-Granja F 1999 Average magnetization and local magnetic moments of Fe_N clusters ($N < 230$) *Phys. Rev.* B **60** 434

[73] Rollmann G, Gruner M E, Hucht A, Entel P, Tiago M L and Chelikowsky J R 2007 Shell-wise Mackay transformation in iron nano-clusters *Phys. Rev. Lett.* **99** 083402

[74] Jensen P J and Bennemann K H 1995 Theory for the atomic shell structure of the cluster magnetic moment and magnetoresistance of a cluster ensemble *Z. Phys.* D **35** 273

[75] Aguilera-Granja F, Montejano-Carrizales J M and Morán-López J L 1998 Magnetic moments of iron clusters: a simple theoretical model *Phys. Lett.* A **242** 255

[76] Xie Y and Blackman J A 2003 On the oscillation of the magnetic moment of free transition metal clusters *J. Phys.: Condens. Matter* **15** L615

[77] Xie Y and Blackman J A 2003 Enhanced effect of magnetic anisotropy on free clusters *Appl. Phys. Lett.* **82** 1446

[78] Gruner M E, Rollmann G, Hucht A and Entel P 2008 Structural and magnetic properties of transition metal nanoparticles from first principles *Advances in Solid State Physics* vol 47, ed R Haug (Berlin: Springer) p 117

[79] Rollmann G 2007 *Ab initio* simulationen eisenhaltiger systeme: vom Festkörper zum cluster *PhD Thesis* Universität Duisburg-Essen

[80] Huber D L 2005 Synthesis, properties, and applications of iron nanoparticles *Small* **1** 482

[81] Ferrando R, Fortunelli A and Johnston R L 2008 Searching for the optimum structures of alloy nanoclusters *Phys. Chem. Chem. Phys.* **10** 640

[82] Pellarin M, Baguenard B, Vialle J L, Lerme J, Broyer M, Miller J and Perez A 1994 Evidence for icosahedral atomic shell structure in nickel and cobalt clusters—comparison with iron clusters *Chem. Phys. Lett.* **217** 349

[83] Mackay A L 1962 A dense non-crystallographic packing of equal spheres *Acta Crystallogr.* **15** 916

[84] Ino S 1969 Stability of multiply-twinned particles *J. Phys. Soc. Japan* **27** 941

[85] Bain E C 1926 The nature of martensite *Trans. AIME* **70** 25

[86] Wulff G 1901 Zur Frage der Geschwindigkeit des Wachsthums und der Auflösung von Krystallflächen *Z. Kristallogr.* **34** 29

[87] Marks L D 1983 Modified Wulff construction for multiply twinned particles *J. Cryst. Growth* **61** 556

[88] Baletto F, Ferrando R, Fortunelli A, Montalenti F and Mottet C 2002 Crossover among structural motifs in transition and noble-metal clusters *J. Chem. Phys.* **116** 3856

[89] Müller M and Albe K 2007 Structural stability of multiply twinned FePt nanoparticles *Acta Mater.* **55** 6617

[90] Herper H C, Hoffmann E and Entel P 1999 *Ab initio* full-potential study of the structural and magnetic phase stability of iron *Phys. Rev.* B **60** 3839

[91] Vystavel T, Palasantzas G, Koch S A and De Hosson J T M 2003 Nanosized iron clusters investigated with *in situ* transmission electron microscopy *Appl. Phys. Lett.* **82** 197

[92] Bobadova-Parvanova P, Jackson K A, Srinivas S and Horoi M 2002 Density-functional investigations of the spin ordering in Fe_{13} clusters *Phys. Rev.* B **66** 195402

[93] Rollmann G, Entel P and Sahoo S 2005 Competing structural and magnetic effects in small iron clusters *Comput. Mater. Sci.* **35** 275–8

[94] Besley N A, Johnston R L, Stace A J and Uppenbrinck J 1995 Theoretical study of the structures and stabilities of iron clusters *J. Mol. Struct.* **341** 75

[95] Chelikowsky J R 2000 The pseudopotential-density functional method applied to nanostructures *J. Phys. D: Appl. Phys.* **33** R33

[96] Gruner M E, Rollmann G, Sahoo S and Entel P 2006 Magnetism of close packed Fe_{147} clusters *Phase Transit.* **79** 701

[97] Baker S H, Asaduzzaman A M, Roy M, Gurman S J, Binns C, Blackman J A and Xie Y 2008 Atomic structure and magnetic moments in cluster-assembled nanocomposite Fe/Cu films *Phys. Rev.* B **78** 014422

[98] Entel P, Gruner M E, Rollmann G, Hucht A, Sahoo S, Zayak A T, Herper H C and Dannenberg A 2008 First-principles investigations of multimetallic transition metal clusters *Phil. Mag.* **88** 2725

[99] Meyer R and Entel P 1998 Martensite–austenite transition and phonon dispersion curves of $Fe_{1-x}Ni_x$ studied by molecular dynamics simulations *Phys. Rev.* B **57** 5140

[100] Entel P, Gruner M E, Hucht A, Meyer R, Rollmann G, Sahoo S and Nayak S K 2008 Simulating structure, magnetism and electronic properties ofmonoatomic, binary and ternary transition metal nanoclusters *IWMNMM-2008: Mesoscopic, Nanoscopic and Macroscopic Materials: Proc. Int. Workshop on Mesoscopic, Nanoscopic and Macroscopic Materials*; *AIP Conf. Proc.* **1063** 3

[101] Wei C M, Cheng C and Chang C 2006 Transition between icosahedral and cuboctahedral nanoclusters of lead *J. Phys. Chem.* B **110** 24642

[102] Lümmen N and Kraska T 2004 Investigation of the formation of iron nanoparticles from the gas phase by molecular dynamics simulation *Nanotechnology* **15** 525

[103] Jónsson H and Andersen H C 1988 Icosahedral ordering in the Lennard-Jones liquid and glass *Phys. Rev. Lett.* **60** 2295

[104] Faken D and Jónsson H 1994 Systematic analysis of local atomic structure combined with 3D computer graphics *Comput. Mater. Sci.* **2** 279

[105] Kübler J 2000 *Theory of Itinerant Electron Magnetism* (Oxford: Oxford University Press)

[106] Ichikawa T 1973 Electron diffraction study of the local atomic arrangement in amorphous iron and nickel films *Phys. Status Solidi* a **19** 707

[107] Suslick K S, Choe S B, Cichowlas A A and Grinstaff M W 1991 Sonochemical synthesis of amorphous iron *Nature* **353** 414

[108] Kovalenko N P, Krasny Y P and Krey U 2001 *Physics of Amorphous Metals* (Berlin: Wiley–VCH)

[109] Apraà E, Baletto F, Ferrando R and Fortunelli A 2004 Amorphization mechanism of icosahedral metal nanoclusters *Phys. Rev. Lett.* **93** 065502

[110] Kar'kina L E, Kar'kin I N and Gornostyrev Y N 2006 Structural transformations in Fe–Ni-alloy nanoclusters: Results of molecular-dynamic-simulation *Phys. Met. Metallogr.* **101** 130

[111] Xie Y and Blackman J A 2004 On the anomalous temperature dependence of the magnetic moment of cobalt clusters *J. Phys.: Condens. Matter* **16** 4373

[112] Xie Y and Blackman J A 2004 Magnetic anisotropy of nanoscale cobalt particles *J. Phys.: Condens. Matter* **16** 3163

[113] Plumer M L, van Ek J and Weller D (ed) 2001 *The Physics of Ultra-High-Density Magnetic Recording* (Berlin: Springer)

[114] Wood R 2009 Future hard disk drive systems *J. Magn. Magn. Mater.* **321** 555

[115] Terris B 2009 Fabrication challenges for patterned recording media *J. Magn. Magn. Mater.* **321** 512

[116] Kodama H, Momose S, Ihara N, Uzumaki T and Atsushi T 2003 Disk substrate deposition techniques for monodisperse chemically sythesized FePt nanoparticle media *Appl. Phys. Lett.* **83** 5253

[117] Perez A, Dupuis V, Tuaillon-Combes J, Bardotti L, Prével B, Bernstein E, Mélinon P, Favre L, Hannour A and Jamet M 2005 Functionalized cluster-assebled magnetic nanostructures for application to high integration-density devices *Adv. Eng. Mater.* **7** 475

[118] Yang X, Liu C, Yu J, Klemmer T, Johns E and Weller D 2004 Fabrications of FePt nanoparticles for self-organized magnetic array *J. Vac. Sci. Technol.* B **22** 31

[119] Held G A, Zeng H and Sun S 2004 Magnetics of ultrathin FePt nanoparticle films *J. Appl. Phys.* **95** 1481

[120] Antoniak C and Farle M 2007 Magnetism at the nanoscale: the case of FePt *Mod. Phys. Lett.* **18** 1111

[121] Lyubina J, Opahle I, Müller K H, Gutfleisch O, Richter M, Wolf M and Schultz L 2005 Magnetocrystalline anisotropy in $L1_0$ FePt and exchange coupling in FePt/Fe_3Pt nanocomposites *J. Phys.: Condens. Matter* **17** 4157

[122] Stappert S, Rellinghaus B, Acet M and Wassermann E F 2003 Gas-phase preparation of $L1_0$ ordered FePt nanoparticles *J. Cryst. Growth* **252** 440

[123] Rellinghaus B, Stappert S, Acet M and Wassermann E F 2003 Magnetic properties of FePt nanoparticles *J. Magn. Magn. Mater.* **266** 142

[124] Stahl B *et al* 2003 Electronic properties of 4 nm FePt particles *Phys. Rev.* B **67** 014422

[125] Salgueiriño Maceira V, Liz-Marzán L M and Farle M 2004 Water-based ferrofluids from Fe_xPt_{1-x} nanoparticles synthesized in organic media *Langmuir* **20** 6946

[126] Held G A, Zeng H and Sun S 2004 Magnetics of ultrathin FePt nanoparticle films *J. Appl. Phys.* **95** 1481

[127] Miyazaki T, Kitakami O, Okamoto S, Shimada Y, Akase Z, Murakami Y, Shindo D, Takahashi Y K and Hono K 2005 Size effect on the ordering of $L1_0$ FePt nanoparticles *Phys. Rev.* B **72** 144419

[128] Dmitrieva O, Rellinghaus B, Kästner J, Liedke M O and Fassbender J 2005 Ion beam induced destabilisation of icosahedral structures in gas phase prepared FePt nanoparticles *J. Appl. Phys.* **97** 10N112

[129] Antoniak C *et al* 2006 Enhanced orbital magnetism in $Fe_{50}Pt_{50}$ nanoparticles *Phys. Rev. Lett.* **97** 117201

[130] Rong C, Li D, Nandwana V, Poudyal N, Ding Y and Wang Z L 2006 Size-dependent chemical and magnetic ordering in $L1_0$-FePt nanoparticles *Adv. Mater.* **18** 2984

[131] Ethirajan A *et al* 2007 A micellar approach to magnetic ultrahigh-density data-storage media: extending the limits of current colloidal methods *Adv. Mater.* **19** 406

[132] Wiedwald U, Klimmer A, Kern B, Han Land Boyen H G, Ziemann P and Fauth K 2007 Lowering of the $L1_0$ ordering temperature of FePt nanoparticles by He^+ ion irradiation *Appl. Phys. Lett.* **90** 062508

[133] Dai Z R, Sun S and Wang Z L 2002 Shapes, multiple twins and surface structures of monodisperse FePt magnetic nanocrystals *Surf. Sci.* **505** 325

[134] Sudfeld D, Dmitrieva O, Friedenberger N, Dumpich G, Farle M, Song C, Kisielowski C, Gruner M E and Entel P 2007 HR-TEM studies of FePt nanoparticles by exit wave reconstruction *Mater. Res. Soc. Symp. Proc.* **998E** 0998-J01-06

[135] Wang R, Dmitrieva O, Farle M, Dumpich G, Ye H Q, Poppa H, Kilaas R and Kisielowski C 2008 Layer resolved

structural relaxation at the surface of magnetic FePt icosahedral nanoparticles *Phys. Rev. Lett.* **100** 017205
[136] Müller M and Albe K 2005 Lattice Monte Carlo simulations of FePt nanoparticles: influence of size, composition, and surface segregation on order–disorder phenomena *Phys. Rev.* B **72** 094203
[137] Yang B, Asta M, Mryasov O N, Klemmer T J and Chantrell R W 2005 Equilibrium Monte Carlo simulations of A1-$L1_0$ ordering in FePt nanoparticles *Scr. Mater.* **53** 417
[138] Yang B, Asta M, Mryasov O N, Klemmer T J and Chantrell R W 2006 The nature of A1-$L1_0$ ordering transition in alloy nanoparticles: a Monte Carlo study *Acta Mater.* **54** 4201
[139] Heinrichs S, Dieterich W and Maass P 2006 Kinetic growth of nano clusters with perpendicular magnetic anisotropy *Europhys. Lett.* **75** 167
[140] Lümmen N and Kraska T 2007 Homogeneous nucleation and growth in iron–platinum vapour investigated by molecular dynamics simulations *Eur. Phys. J.* D **41** 247
[141] Rossi G, Ferrando R and Mottet C 2008 Structure and chemical ordering in CoPt nanoalloys *Faraday Discuss.* **138** 193
[142] Penuelas J, Andreazza-Vignolle C, Andreazza P, Ouerghi A and Bouet N 2008 Temperature effect on the ordering and morphology of CoPt nanoparticles *Surf. Sci.* **602** 545
[143] Creuze J, Braems I, Berthier F, Mottet C, Tréglia G and Legrand B 2008 Model of surface segregation driving forces and their coupling *Phys. Rev.* B **78** 075413
[144] Fortunelli A and Velasco A M 1999 Structural and electronic properties of Pt/Fe nanoclusters from EHT calculations *J. Mol. Struct. (Theochem)* **487** 251
[145] Fortunelli A and Velasco A M 2000 Local properties of PT/FE nanoclusters by EHT calculations *J. Mol. Struct. (Theochem)* **528** 1
[146] Wang Y, Stocks G M, Rusanu A, Nicholson D M C, Eisenbach M, Zhang Q and Liu J P 2007 Electronic and magnetic structure of $L1_0$-FePt nanoparticle embedded in FePt random alloy *IEEE Trans. Magn.* **43** 3103
[147] Gruner M E, Rollmann G, Entel P and Farle M 2008 Multiply twinned morphologies of Fe–Pt and Co–Pt nanoparticles *Phys. Rev. Lett.* **100** 087203
[148] Gruner M E 2008 Antiferromagnetism and segregation in cuboctahedral FePt nanoparticles *J. Phys. D: Appl. Phys.* **41** 134015
[149] Entel P and Gruner M E 2009 Large-scale *ab initio* simulations of binary transition metal clusters for storage media materials *J. Phys.: Condens. Matter* **21** 064228
[150] Cheng D, Wang W and Huang S 2006 The onion-ring structure for Pd–Pt bimetallic clusters *J. Phys. Chem.* B **110** 16193
[151] Calvo F 2008 Solid-solution precursor to melting in onion-ring Pd–Pt nanoclusters: a case of second-order-like phase change? *Faraday Discuss.* **138** 75
[152] Cheng D and Cao D 2008 Structural transition and melting of onion-ring Pd–Pt bimetallic clusters *Chem. Phys. Lett.* **461** 71
[153] Clark J F, Pinski F J, Johnson D D, Sterne P A, Staunton J B and Ginatempo B 1995 van Hove singularity induced $L1_1$ ordering in CuPt *Phys. Rev. Lett.* **74** 3225
[154] Lyubina J, Opahle I, Richter M, Gutfleisch O, Müller K H, Schultz L and Isnard O 2006 Influence of composition and order on the magnetism of Fe–Pt alloys: neutron powder diffraction and theory *Appl. Phys. Lett.* **89** 032506
[155] Zeng H, Sabirianov R, Mryasov O, Yan M L, Cho K and Sellmyer D J 2002 Curie temperature of FePt:B_2O_3 nanocomposite films *Phys. Rev.* B **66** 184425
[156] Brown G, Kraczek B, Janotti A, Schulthess T C, Stocks G M and Johnson D D 2003 Competition between ferromangetism and antiferromagnetism in FePt *Phys. Rev.* B **68** 052405
[157] Mryasov O N 2004 Magnetic interactions in 3d–5d layered ferromagnets *J. Magn. Magn. Mater.* **272** 800
[158] MacLaren J M, Duplessis R R, Stern R A and Willoughby S 2005 First principles calculations of FePt, CoPt, Co_3Pt, and Fe_3Pt alloys *IEEE Trans. Magn.* **41** 4347
[159] Mryasov O N 2005 Magnetic interactions and phase transformations in FeM, M = (Pt, Rh) ordered alloys *Phase Transit.* **78** 197
[160] Fallot M 1938 Les alliages du fer avec les métaux de la famille du platine *Ann. Phys.* **10** 291
[161] Mryasov O N, Nowak U, Guslienko K Y and Chantrell R W 2005 Temperature-dependent magnetic properties of FePt: effective spin Hamiltonian model *Europhys. Lett.* **69** 805
[162] Tu P, Heeger A J, Kouvel J S and Comly J B 1969 Mechanism for the first-order magnetic transition in the FeRh system *J. Appl. Phys.* **40** 1368
[163] Gruner M E, Hoffmann E and Entel P 2003 Instability of the rhodium magnetic moment as origin of the metamagnetic phase transition in α-FeRh *Phys. Rev.* B **67** 064415
[164] Ju G, Hohlfeld J, van de Veerdonk R J M, Mryasov O N, Kim J Y, Wu X, Weller D and Koopmanns B 2004 Ultrafast generation of ferromagnetic order via a laser-induced phase transformation in FeRh thin films *Phys. Rev. Lett.* **93** 197403
[165] Gruner M E and Dannenberg A 2009 Structure and magnetism in near-stoichiometric FePd nanoparticles *J. Magn. Magn. Mater.* **321** 861
[166] Tournus F, Tamion A, Blanc N, Hannour A, Bardotti L, Prével B, Ohresser P, Bonet E, Epicier T and Dupuis V 2008 Evidence of $L1_0$ chemical order in CoPt nanoclusters: direct observation and magnetic signature *Phys. Rev.* B **77** 144411
[167] Boyen H G *et al* 2005 Electronic and magnetic properties of ligand-free FePt nanoparticles *Adv. Mater.* **17** 574
[168] Planes A, Mañosa L and Acet M 2009 Magnetocaloric effect and its relation to shape memory properties in ferromagnetic Heusler alloys *J. Phys.: Condens. Matter* **21** 233201
[169] Ullakko K, Huang J K, Kantner C, O'Handley R C and Kokorin V V 1996 Large magnetic-field-induced strains in Ni_2MnGa single crystals *Appl. Phys. Lett.* **69** 1966
[170] Sozinov A, Likhachev A A, Lanska N and Ullakko K 2002 Giant magnetic-field-induced strain in NiMnGa seven-layered martensitic phase *Appl. Phys. Lett.* **80** 1746
[171] Chernenko V, Segui C, Cesari E, Pons J and Kokorin V 1998 Sequence of martensitic transformations in Ni–Mn–Ga alloys *Phys. Rev.* B **57** 2659
[172] Khovaylo V V, Buchelnikov V D, Kainuma R, Koledov V V, Ohtsuka M, Shavrov V G, Takagi T, Taskaev S V and Vasiliev A N 2005 Phase transitions in $Ni_{2+x}Mn_{1-x}Ga$ with a high Ni excess *Phys. Rev.* B **72** 224408
[173] Richard M, Feuchtwanger J, Schlagel D, Lograsso T, Allen S and O'Handley R 2006 Crystal structure and transformation behavior of Ni–Mn–Ga martensites *Scr. Mater.* **54** 1797
[174] Enkovaara J, Ayuela A, Nordström L and Nieminen R M 2002 Magnetic anisotropy in Ni_2MnGa *Phys. Rev.* B **65** 134422
[175] Fähler S 2007 An introduction to actuation mechanisms in magnetic shape memory alloys *ECS Trans.* **3** 155
[176] Krenke T, Acet M, Wassermann E F, Moya X, Mañosa L and Planes A 2006 Ferromagnetism in the austenitic and martensitic states of Ni–Mn–In alloys *Phys. Rev.* B **73** 174413
[177] Krenke T, Duman E, Acet M, Wassermann E F, Moya X, Mañosa L, Planes A, Suard E and Ouladdiaf B 2007 Magnetic superelasticity and inverse magnetocaloric effect in Ni–Mn–In *Phys. Rev.* B **75** 104414

[178] James R D and Wuttig M 1998 Magnetostriction of martensite *Phil. Mag.* A **77** 1273

[179] Cui J, Shield T W and James R D 2004 Phase transformation and magentic anisotropy of an iron–palladium ferromagnetic shape-memory alloy *Acta Mater.* **52** 35

[180] Hayashi R, Murray S, Marioni M, Allen S and O'Handley R 2000 Magnetic and mechanical properties of FeNiCoTi magnetic shape memory alloy *Sensors Actuators* **81** 219

[181] Kakeshita T and Fukuda T 2002 Giant magnetostriction in Fe_3Pt and FePd ferromagnetic shape memory alloys *Mater. Sci. Forum* **394/395** 531

[182] Fukuda T, Sakamoto T, Kakeshita T, Takeuchi T and Kishio K 2004 Rearrangement of martensite variants in iron-based ferromagnetic shape memory alloy under magnetic field *Mater. Trans.* **45** 188

[183] Kakeshita T, Fukuda T and Takeuchi T 2006 Magneto-mechanical evaluation for twinning plane movement driven by magnetic field in ferromagnetic shape memory alloys *Mater. Sci. Eng.* A **438–440** 12

[184] Opahle I, Koepernik K, Nitzsche U and Richter M 2009 Jahn-teller like origin of the tetragonal distortion in disordered Fe–Pd magnetic shape memory alloys *Appl. Phys. Lett.* **94** 072508

[185] Stern R A, Willoughby S D, Ramirez A, MacLaren J M, Cui J, Pan Q and James R D 2002 Electronic and structural properties of Fe_3Pd-Pt ferromagnetic shape memory alloys *J. Appl. Phys.* **91** 7818

[186] Stern R A, Willoughby S D, MacLaren J M, Cui J, Pan Q and James R D 2003 Fe_3Pd ferromagnetic shape memory alloys *J. Appl. Phys.* **93** 8644

[187] Brown P J, Bargawi A Y, Crangle J, Neumann K U and Ziebeck K R A 1999 Direct observation of a band Jahn–Teller effect in the martensitic phase transition of Ni_2MnGa *J. Phys.: Condens. Matter* **11** 4715

[188] Ayuela A, Enkovaara J, Ullakko K and Nieminen R 1999 Structural properties of magnetic Heusler alloys *J. Phys.: Condens. Matter* **11** 2017

[189] Godlevsky V and Rabe K 2001 Soft tetragonal distortions in ferromagnetic Ni_2MnGa and related materials from first principles *Phys. Rev.* B **63** 134407

[190] Ayuela A, Enkovaara J and Nieminen R M 2002 *Ab initio* study of tetragonal variants in Ni_2MnGa alloy *J. Phys.: Condens. Matter* **14** 5325

[191] Enkovaara J, Ayuela A, Jalkanen J, Nordström L and Nieminen R M 2003 First-principles calculations of spin spirals in Ni_2MnGa and Ni_2MnAl *Phys. Rev.* B **67** 544171

[192] Zayak A T, Adeagbo W A, Entel P and Rabe K M 2006 e/a dependence of the lattice instability of cubic Heusler alloys from first principles *Appl. Phys. Lett.* **88** 111903

[193] Banik S *et al* 2007 Structural studies of $Ni_{2+x}Mn_{1-x}Ga$ by powder x-ray diffraction and total energy calculations *Phys. Rev.* B **75** 104107

[194] Gruner M E, Adeagbo W A, Zayak A T, Hucht A, Buschmann S and Entel P 2008 Influence of magnetism on the structural stability of cubic $L2_1$ Ni_2MnGa *Eur. Phys. J. Special Topics* **158** 193

[195] Zayak A, Entel P and Chelikowsky J 2008 Minority-spin polarization and surface magnetic enhancement in Heusler clusters *Phys. Rev.* B **77** 212401

[196] Zayak A T, Beckman S P, Tiago M L, Entel P and Chelikowsky J R 2008 Switchable Ni–Mn–Ga Heusler nanocrystals *J. Appl. Phys.* **104** 074307

[197] Kart S, Uludogan M, Karaman I and Cagin T 2008 DFT studies on structure, mechanics and phase behavior of magnetic shape memory alloys: Ni_2MnGa *Phys. Status Solidi* a **205** 1026

[198] Velikokhatnyi O I and Naumov I I 1999 Electronic structure and instability of Ni_2MnGa *Fiz. Tverd. Tela* **41** 684
Velikokhatnyi O I and Naumov I I 1999 *Phys. Solid State* **41** 617

[199] Lee Y, Rhee J Y and Harmon B N 2002 Generalized susceptibility of the magnetic shape-memory alloy Ni_2MnGa *Phys. Rev.* B **66** 054424

[200] Bungaro C, Rabe K M and Dal Corso A 2003 First-principles study of lattice instabilities in ferromagnetic Ni_2MnGa *Phys. Rev.* B **68** 134104

[201] MacLaren J M 2002 Role of alloying on the shape memory effect in Ni_2MnGa *J. Appl. Phys.* **91** 7801

[202] Entel P, Gruner M E, Adeagbo W A, Eklund C J, Zayak A T, Akai H and Acet M 2007 *Ab initio* modeling of martensitic transformations (MT) in magnetic shape memory alloys *J. Magn. Magn. Mater.* **310** 2761

[203] Opeil C P *et al* 2008 Combined experimental and theoretical investigation of the premartensitic transition in Ni_2MnGa *Phys. Rev. Lett.* **100** 165703

[204] Entel P, Buchelnikov V D, Gruner M E, Hucht A, Khovailo V V, Nayak S K and Zayak A T 2008 Shape memory alloys: a summary of recent achievements *Mater. Sci. Forum* **583** 21

[205] Enkovaara J, Ayuela A, Nordström L and Nieminen R M 2002 Structural, thermal, and magnetic properties of Ni_2MnGa *J. Appl. Phys.* **91** 7798

[206] Zayak A T, Entel P, Enkovaara J, Ayuela A and Nieminen R M 2003 A first-principles investigation of phonon softenings and lattice instabilities in the shape-memory system Ni_2MnGa *Phys. Rev.* B **68** 132402

[207] Zayak A T, Entel P, Rabe K M, Adeagbo W A and Acet M 2005 Anomalous vibrational effects in nonmagnetic and magnetic Heusler alloys *Phys. Rev.* B **72** 0541113

[208] Zayak A T and Entel P 2005 A critical discussion of calculated modulated structures, Fermi surface nesting and phonon softening in magnetic shape memory alloys Ni_2Mn (Ga, Ge, Al) and Co_2Mn (Ga, Ge). *J. Magn. Magn. Mater.* **290/291** 874

[209] Entel P, Gruner M E, Adeagbo W A and Zayak A 2008 Magnetic field-induced changes in magnetic shape memory alloys *Mater. Sci. Eng.* A **481/482** 258

[210] Uijttewaal M A, Hickel T, Neugebauer J, Gruner M E and Entel P 2009 Understanding the phase transitions of the Ni_2MnGa magnetic shape memory system from first principles *Phys. Rev. Lett.* **102** 035702

[211] Zheludev A, Shapiro S, Wochner P, Schwartz A, Wall M and Tanner L 1995 Phonon anomaly, central peak, and microstructures in Ni_2MnGa *Phys. Rev.* B **51** 11310

[212] Zheludev A, Shapiro S, Wochner P and Tanner L 1996 Precursor effects and premartensitic transformation in Ni_2MnGa *Phys. Rev.* B **54** 15045

[213] Stuhr U, Vorderwisch P, Kokorin V and Lindgard P A 1997 Premartensitic phenomena in the ferro- and paramagnetic phases of Ni_2MnGa *Phys. Rev.* B **56** 14360

[214] Manosa L, Planes A, Zarestky J, Lograsso T, Schlagel D and Stassis C 2001 Phonon softening in Ni–Mn–Ga alloys *Phys. Rev.* B **64** 024305

[215] Moya X, Mañosa L, Planes A, Krenke T, Acet M, Garlea V O, Lograsso T A, Schlagel D L and Zarestky J L 2006 Lattice dynamics and phonon softening in Ni–Mn–Al Heusler alloys *Phys. Rev.* B **73** 064303

[216] Shapiro S M, Vorderwisch P, Habicht K, Hradil K and Schneider H 2006 Observations of phasons in magnetic shape memory alloy Ni_2MnGa *Europhys. Lett.* **77** 56004

[217] Entel P, Gruner M E and Hucht A 2008 A first-principles study of the martensitic instabilities in magnetic shape memory alloys *Mater. Res. Soc. Symp. Proc.* **1050E** 1050-BB03–1

[218] Varma C M and Weber W 1977 Phonon dispersion in transition metals *Phys. Rev. Lett.* **39** 1094

[219] Varma C M and Weber W 1979 Phonon dispersion in transition metals *Phys. Rev.* B **19** 6142

[220] Moruzzi V L, Marcus P M, Schwarz K and Mohn P 1986 Ferromagnetic phases of bcc and fcc Fe, Co, and Ni *Phys. Rev.* B **34** 1784

[221] Bhattacharya K 2003 *Microstructure of Martensite—Why it Forms and How it Gives Rise to the Shape-Memory Effect* (Oxford: Oxford University Press)
[222] Gruner M E, Entel P, Opahle I and Richter M 2008 *Ab initio* investigation of twin boundary motion in the magnetic shape memory Heusler alloy Ni_2MnGa *J. Mater. Sci.* **43** 3825
[223] Ball J M and James R D 1987 Fine phase mixtures as minimizers of energy *Arch. Ration. Mech. Anal.* **100** 13
[224] Pitteri M and Zanzotto G 2003 *Continuum Models for Phase Transitions and Twinning in Crystals* (Boca Raton, FL: Chapman and Hall/CRC)
[225] Brown P J, Dennis B, Crangle J, Kanomata T, Matsumoto M, Neumann K U, Justham L M and Ziebeck K R A 2004 Stability of martensitic domains in the ferromagnetic alloy Ni_2MnGa: a mechanism for shape memory behaviour *J. Phys.: Condens. Matter* **16** 65
[226] Okamoto N, Fukuda T, Kakeshita T and Takeuchi T 2006 Magnetocrystalline anisotropy constant and twinning stress in martensite phase of Ni–Mn–Ga *Mater. Sci. Eng.* A **438–440** 948
[227] Kakeshita T and Fukuda T 2006 Energy evaluation for twinning plane movement in ferromagnetic shape memory alloys *Int. J. Appl. Electron.* **23** 45
[228] Pond R C and Celotto S 2003 Special interfaces: military transformations *Int. Mater. Rev.* **48** 225
[229] Müllner P and Kostorz G 2008 Microstructure of magnetic shape-memory alloys: between magnetoelasticity and magnetoplasticity *Mater. Sci. Forum* **583** 43
[230] Kokalj A 2003 Computer graphics and graphical user interfaces as tools in simulations of matter at the atomic scale *Comput. Mater. Sci.* **28** 155 http://www.xcrysden.org
[231] www.psi-k.org